Current-Induced Modulation of the Ocean Wave Spectrum and the Role of Nonlinear Energy Transfer

HITOSHI TAMURA

Frontier Research Center for Global Change, Japan Agency for Marine-Earth Science and Technology, Yokohama, Kanagawa, Japan

TAKUJI WASEDA

Department of Environmental and Ocean Engineering, University of Tokyo, Tokyo, and Frontier Research Center for Global Change, Japan Agency for Marine-Earth Science and Technology, Yokohama, Kanagawa, Japan

YASUMASA MIYAZAWA

Frontier Research Center for Global Change, Japan Agency for Marine-Earth Science and Technology, Yokohama, Kanagawa, Japan

KOSEI KOMATSU

National Research Institute of Fisheries Science, Fisheries Research Agency, Yokohama, Japan

(Manuscript received 14 February 2008, in final form 15 June 2008)

ABSTRACT

Numerical simulations were performed to investigate current-induced modulation of the spectral and statistical properties of ocean waves advected by idealized and realistic current fields. In particular, the role of nonlinear energy transfer among waves in wave–current interactions is examined. In this type of numerical simulation, it is critical to treat the nonlinear transfer function (Snl) properly, because a rigorous Snl algorithm incurs a huge computational cost. However, the applicability of the widely used discrete interaction approximation (DIA) method is strictly limited for complex wave fields. Therefore, the simplified RIAM (SRIAM) method is implemented in an operational third-generation wave model. The method approximates an infinite resonant quadruplet with 20 optimized resonance configurations. The performance of the model is assessed by applying it to fetch-limited wave growth and wave propagation against a shear current. Numerical simulations using the idealized current field revealed that the Snl retained spectral form by redistributing the refracted wave energy; this suggests that energy concentration due to ray focusing is dispersed via the self-stabilization effect of nonlinear transfer. A hindcast simulation using wind and current reanalysis data indicated that the difference in the average monthly wave height was substantial and that instantaneous wave–current interactions were highly sensitive to small current structures. Spectral shape was also modulated, and the spatial distributions of the directional bandwidth with or without current data were completely different. Moreover, the self-stabilization effect of the Snl was also confirmed in a realistic situation. These results indicate that a realistic representation of the current field is crucial for high-resolution wave forecasting.

1. Introduction

When random or directional ocean waves propagate through a current field that varies spatially, their statistical properties, such as significant wave height or mean wave direction, can be modulated. In general, changes in wave characteristics are attributed to physical processes of wave refraction and/or straining (Holthuijsen and Tolman 1991) caused by the horizontal shear current. Recent studies using spaceborne altimeter data have indicated that strong ocean currents, such as the Kuroshio of the Pacific Ocean, exert a significant influence on wave characteristics (Hwang 2005); similar observations have been reported for a wide range of temporal and spatial scales (Tolman 1991; Wang et al. 1994;

Corresponding author address: Hitoshi Tamura, 3173-25 Showa-machi, Kanazawa-Ku, Yokohama, Kanagawa 236-0001, Japan.
E-mail: htamura@jamstec.go.jp

DOI: 10.1175/2008JPO4000.1

Masson 1996). Moreover, wave–current interactions may generate so-called freak waves of extreme size (e.g., White and Fornberg 1998), as abnormal waves have been observed repeatedly in areas with strong currents (e.g., Lavrenov 1998). Therefore, the ability to accurately estimate the effects of currents on waves, and include wave–current interactions, is crucial for wave hindcasting and forecasting.

Wave–current interactions have mainly been investigated within the framework of linear theory based on the wave-ray model (e.g., Kenyon 1971; Mei 1989) or the propagation equation of wave-action density (e.g., Tolman 1990; Jonsson 1990; Hubbert and Wolf 1991). These studies provided us with a good understanding of the mechanisms of ray focusing, spectral modulation, and energy convergence due to wave refraction and/or straining. When unidirectional waves or waves with relatively mild slopes propagate in a calm sea without wind input or white capping, these methods are reasonable for analyzing the modulation of wave energy induced by currents. However, under more realistic oceanic conditions, it is necessary to consider the many physical features and processes of waves, such as nonlinearity, multidirectionality, and wave growth and decay. To this end, third-generation wave models provide the most powerful research tool for investigating wave–current interactions (Holthuijsen and Tolman 1991; Komen et al. 1994), because they describe the temporal and spatial evolution of the wave spectrum without any prior assumptions about spectral shape. The probability of freak- wave occurrence is strongly related to wave spectral shape, which is characterized by wave steepness, frequency, and directional bandwidth (Janssen 2003; Onorato et al. 2004; Waseda et al. 2009). Therefore, we expect that accurate evaluation of spectral shape will lead to improved predictions of abnormal waves.

Despite numerous studies on current-induced modulation of wave characteristics, few have addressed changes in spectral shape. This is in large part due to the complexity of calculating nonlinear energy transfer in resonant four-wave interactions or resonant quadruplets. Among the source terms of third-generation wave models, the nonlinear transfer function (Snl) is the most important element controlling the evolution of wave spectra, such as the down shifting of the spectral peak and the self-stabilization of the spectral form (Resio and Perrie 1991; Young and Van Vledder 1993; Komatsu and Masuda 1996). The most widely used method for evaluating Snl is the discrete interaction approximation (DIA) method (Hasselmann et al. 1985), because of its low computational cost. However, DIA is inadequate for calculating the energy transfer of bimodal wave spectra or even standardized wave spectra, such as the Joint North Sea Wave Observation Project (JONSWAP) spectrum (e.g., Komatsu and Masuda 1996; Van Vledder 2006), because the method can include only a low number of quadruplets. Precise evaluation of nonlinear transfer requires a large number of quadruplets (e.g., Masuda 1980; Van Vledder 2006). Such calculations incur huge computational costs, making rigorous simulation of realistic wave–current coupling impossible. Therefore, despite advances in computer technology, such methods have been limited to idealized test cases, such as duration- or fetch-limited wave growth. Because of this lack of a reasonable method for computing Snls, the effect of nonlinearity on shear current-induced wave evolution has never been studied. Additionally, although many studies have investigated the role of nonlinear transfer in the frequency domain (Resio and Perrie 1991; Young and Van Vledder 1993; Komatsu and Masuda 1996), little is known about its effects in the directional domain.

We investigated the impact of the Snl on the wave spectrum in several complex situations. We also attempted to identify the current-induced modulation of the spectral and statistical properties of ocean waves using a third-generation wave model. In particular, we assessed the role of nonlinear transfer in wave–current interactions. To accurately evaluate Snl with lower computational costs, we used the simplified RIAM (SRIAM) method (Komatsu 1996), which was developed for operational wave forecasting. SRIAM reduces computational costs considerably by utilizing 20 resonance configurations that retain the general properties of the Snl kernel function. Komatsu (1996) showed that SRIAM compared favorably with the rigorous RIAM method for duration-limited wave growth after an abrupt change in wind direction and the evolution of perturbed-equilibrium spectra. However, little is known about the applicability of SRIAM to a more complex wave field.

In the following section, we briefly describe SRIAM, its applicability to some wave spectra and fetch-limited growth of wind waves, and its accuracy compared to RIAM. In section 3, we examine current-induced changes in wave properties for an idealized current field and identify the role of nonlinear transfer in wave–current interactions. In section 4, we present the findings of a hindcast simulation using wind and current reanalysis data to investigate the impact of the Kuroshio on nearby waves. Finally, we present our conclusions in section 5.

TABLE 1. Eight test spectra used for the optimization of SRIAM; peakedness factor γ and directional spreading s.

j	γ	s
1	1.0	2
2	1.0	10
3	3.3	2
4	3.3	10
5	5.0	2
6	5.0	10
7	9.0	2
8	9.0	10

2. The basic properties of SRIAM

a. A brief introduction to SRIAM

Theoretically, there are an infinite number of possible four-wave configurations that satisfy resonance conditions. Thus, it is critical to identify how many resonance configurations are necessary to approximate the nonlinear transfer function reasonably well for a given wave spectrum. DIA assumes that the interactions among neighboring wavenumbers reproduce the principal features of nonlinear transfer (Hasselmann et al. 1985). Based on kernel function analysis, the strength of a resonant interaction is generally weak for four waves having large differences in their wavenumber vectors (Masuda 1980). Moreover, by discarding resonance configurations that exceeded the threshold of the specific wavenumber ratio, Komatsu and Masuda (1996) successfully reduced the required number of resonant four-wave combinations without losing accuracy. In kernel function analysis, quasi-singular quadruplets contribute the most to nonlinear transfer, whereas regular quadruplets are expected to contribute far less. By selecting only from the quasi-singular quadruplets, it is possible to reduce the number of resonance configurations included in the calculation. SRIAM uses 20 resonance configurations with RIAM-based optimization; its computational cost is 100 times less than that of RIAM (20 times more than DIA).

Komatsu (1996) identified 20 optimized quadruplets that represent the infinite number of possible resonant four-wave configurations. Interaction coefficients were specified using RIAM for specific JONSWAP-type test wave spectra with peakedness factor γ and $\cos^s\theta$-type directional spreading, where γ and s are as defined in Table 1 (reproduced here from Komatsu 1996). The configurations used in SRIAM are shown in Fig. 1. Wavenumber vectors $\mathbf{k}_1$, $\mathbf{k}_2$, $\mathbf{k}_3$, and $\mathbf{k}_4$ for one quadruplet are indicated by arrows. Other quadruplets are specified with the symbols ○ and +, which represent the end points of wavenumber vectors $\mathbf{k}_1$ and $\mathbf{k}_3$, respectively. Mirror images of these configurations were also considered but are not shown in the figure. All sets of quadruplets that satisfy the resonance conditions lie on a specific curve γ_{conf} = constant (Masuda 1980). Table 2 (reproduced here from Komatsu 1996) shows the detailed parameters that determine each resonant configuration and the associated interaction coefficients, where i_{rep} is the number of resonant configurations, $\tilde{\theta}_1$ and $\tilde{\theta}_3$ are wavenumber vector angles, $\tilde{\sigma}_3$ is the ratio of angular frequencies σ_3 and σ_4, $\tilde{K}$ is the kernel function for a specific quadruplet, and C_{irep} is a parameter that modifies the interaction coefficient so that an optimized kernel function is evaluated via $C_{\text{irep}} \times \tilde{K}$.

b. Implementation of SRIAM in an operational wave model

We implemented SRIAM in WAVEWATCH-III (WW3; Tolman 2002), an operational third-generation wave model developed and maintained by the National Oceanic and Atmospheric Administration (NOAA; http://polar.ncep.noaa.gov/waves). We considered three numerical points of view for implementing SRIAM in the default WW3 model.

(i) Typical operational wave models, including WW3, apply a parametric spectral tail beyond a dynamically adjusted cutoff frequency to reduce computational cost. However, we did not apply this type of cutoff frequency and spectral tail. Spectral evolution and the wave growth rate strongly depend on cutoff frequency and a constrained tail (Tolman 1992; Banner and Young 1994; Bidlot et al. 2007). On the other hand, the spectral tail is necessary for computing the Snl when the highest frequency corresponding to the resonant four waves is larger than the highest discrete model frequency. Therefore, we assumed an f^{-5} spectral tail outside the model frequency range (greater than 0.414 Hz) as used in the default setting of the WW3.

(ii) For time integration of the energy balance equation, a semi-implicit scheme is typically used (WAMDI Group 1988; Komen et al. 1994). This method reduces the Jacobian matrix of the functional derivative using only its diagonal terms. However, applying this method to SRIAM and RIAM does not lead to reasonable wave spectra (as will be seen in the appendix). Therefore, we used the implicit scheme (Lavrenov 2003), the details of which are provided in the appendix.

(iii) For all calculations, we used a fixed spectral resolution and the same source functions of wind input and dissipation because the purpose of this study is to investigate the impact of the nonlinear transfer function Snl on the wave spectrum. The spectral

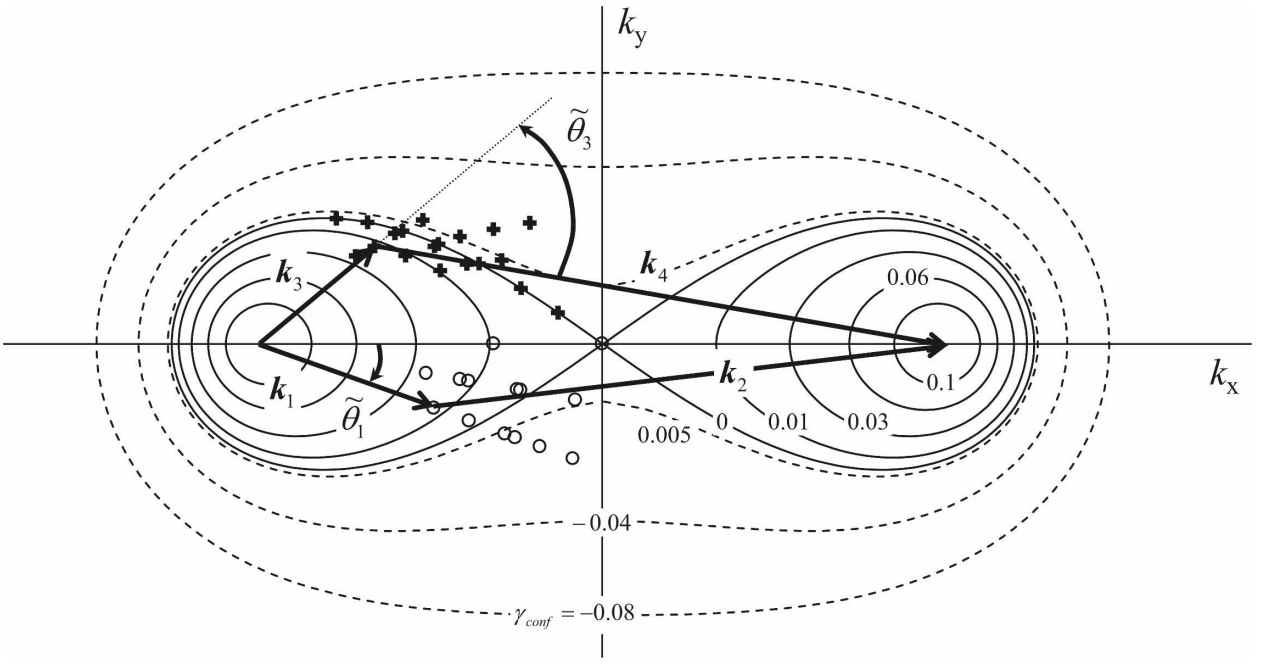

FIG. 1. The interaction diagram of the wavenumber plane with the resonance configurations used in SRIAM: contours of γ_{conf} are as defined by Masuda (1980). Wavenumber vectors $\mathbf{k}_1$, $\mathbf{k}_2$, $\mathbf{k}_3$, and $\mathbf{k}_4$ of one quadruplet are indicated by arrows. Other quadruplets are specified with the symbols ○ and +, which represent the end points of the wavenumber vectors $\mathbf{k}_1$ and $\mathbf{k}_3$, respectively.

space was discretized using 25 frequencies ranging from 0.042 to 0.414 (relative frequency of 10%) with 36 directions ($\Delta\theta = 10°$). Tolman and Chalikov's (1996) wave-growth and decay source terms were used, and stable stratification of the atmospheric boundary layer was assumed.

TABLE 2. Parameters determining the resonant configurations and the associated interaction coefficients for SRIAM: singular quadruplets (i_{rep}: 1–7) and regular quadruplets (i_{rep}: 8–20).

i_{rep}	$\tilde{\theta}_1$	$\tilde{\sigma}_3$	$\tilde{\theta}_3$	γ_{conf}	$\log_{10} \tilde{K}$	C_{irep}
1	0	0.88	10	0.000	2.15	1.00
2	0	0.78	20	0.000	1.85	1.00
3	0	0.70	30	0.000	1.11	1.00
4	0	0.63	40	0.000	0.40	1.00
5	0	0.57	50	0.000	−0.29	1.00
6	0	0.52	60	0.000	−0.92	1.00
7	0	0.49	70	0.000	−1.51	1.00
8	0	0.62	30	0.009	−0.64	2.01
9	10	0.75	30	−0.004	0.98	1.96
10	10	0.68	30	0.002	0.01	1.94
11	10	0.62	40	0.001	−0.56	1.96
12	10	0.56	40	0.011	−1.46	4.60
13	10	0.51	50	0.013	−2.04	8.44
14	10	0.47	50	0.024	−2.80	2.63
15	20	0.83	40	−0.018	0.93	2.01
16	20	0.75	40	−0.013	0.38	1.62
17	20	0.68	40	−0.006	−0.28	1.79
18	20	0.62	50	−0.008	−1.00	2.67
19	20	0.56	50	0.002	−1.56	1.57
20	20	0.51	50	0.013	−2.25	1.53

c. *Comparison of the nonlinear transfer functions*

The simplest and least ambiguous way to validate each model was to estimate the Snl directly from a given wave spectrum. To investigate the accuracy of SRIAM, we compared it to the Snls obtained by RIAM and DIA. In the DIA calculation, the interaction coefficient was set to 1×10^7, as used in WW3, instead of the 2.8×10^7 used in the wave model (WAM; WAMDI Group 1988), to avoid overestimating transfer toward higher frequencies (Tolman and Chalikov 1996). Figure 2 compares the one-dimensional distribution of Snls calculated by SRIAM, RIAM, and DIA for each spectrum. The wave spectra examined were (i) a Pierson–Moskowitz spectrum with $\cos^{10}\theta$ directional spreading, (ii) the standard JONSWAP spectrum with $\cos^2\theta$ directional spreading, (iii) a double-peaked spectrum in the frequency domain ($f_{p1} = 0.1$ Hz, $f_{p2} = 0.13$ Hz) with $\cos^2\theta$ directional spreading, and (iv) a double-peaked spectrum ($f_{p1} = 0.1$ Hz, $f_{p2} = 0.2$ Hz) with $\cos^2\theta$ directional spreading.

SRIAM properly represented nonlinear transfer in shape and magnitude for cases (i) and (ii). This is because SRIAM was optimized for the eight test spectra indicated in Table 1, which included the wave spectra of (i) and (ii). Moreover, Figs. 2c,d indicate that SRIAM reproduced nonlinear transfer for the bimodal wave spectra, which were not used for optimization. These results imply that SRIAM has practical applicability in

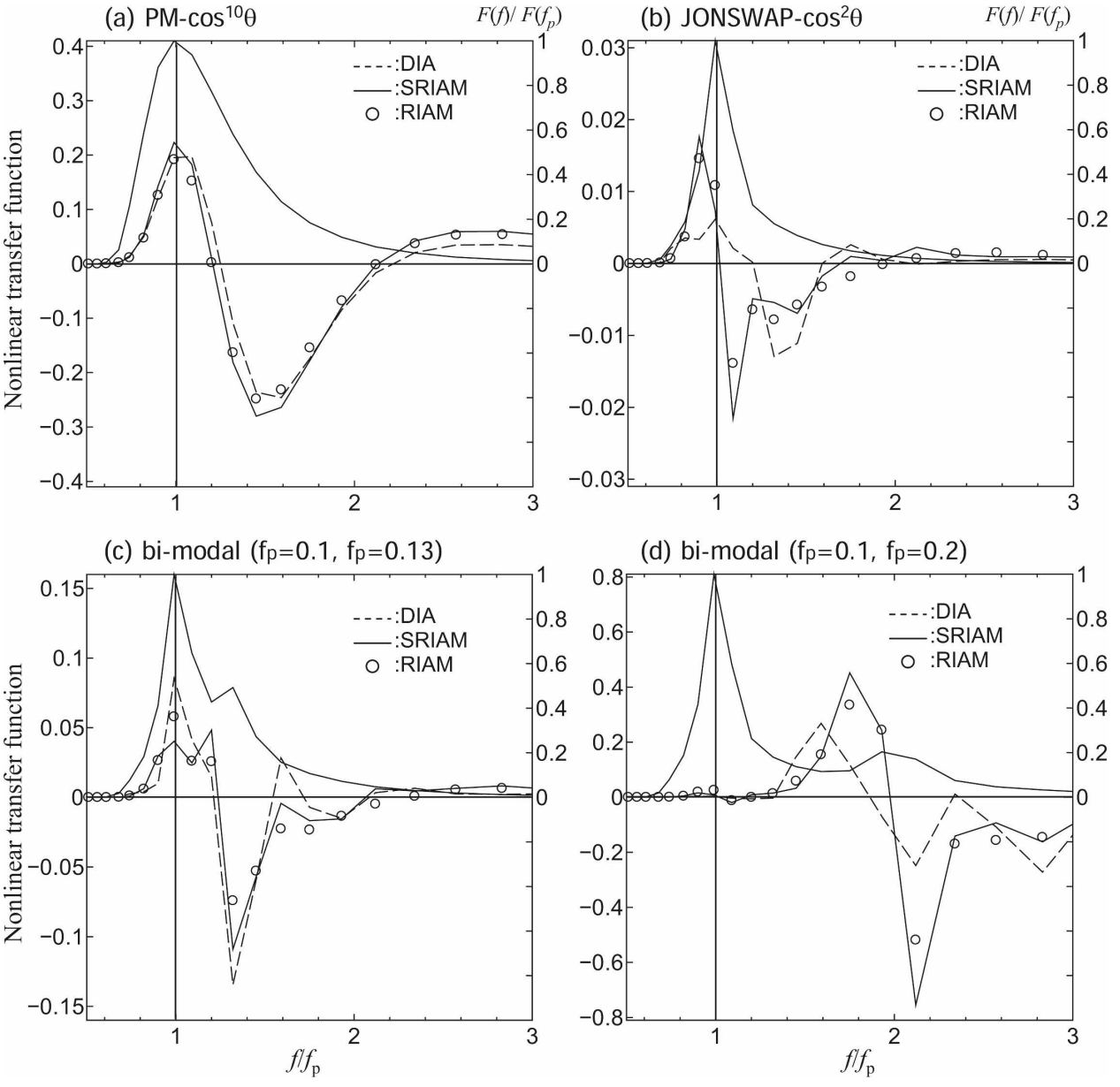

FIG. 2. Comparison of the one-dimensional nonlinear transfer functions obtained by SRIAM, RIAM, and DIA for each spectrum. The wave spectra examined are (a) Pierson–Moskowitz spectrum with $\cos^{10}\theta$ directional spreading, (b) standard JONSWAP spectrum with $\cos^2\theta$ directional spreading, (c) a double-peaked spectrum in the frequency domain (f_{p1} = 0.1 Hz, f_{p2} = 0.13 Hz) with $\cos^2\theta$ directional spreading, and (d) a double-peaked spectrum (f_{p1} = 0.1 Hz, f_{p2} = 0.2 Hz) with $\cos^2\theta$ directional spreading.

complex situations, while DIA is deficient, especially for the JONSWAP spectrum and the double-peaked spectra indicated in Figs. 2b,d, respectively.

The different roles of nonlinear transfer were confirmed in the two cases of bimodal wave spectra that depended on the ratio between peak frequencies. When the ratio of the two peak frequencies was small, as indicated in Fig. 2c, negative and positive peak values of nonlinear transfer appeared at the high- and low-frequency peaks, respectively. The profile of the Snl suggests that nonlinear interactions induce energy flows that smooth the perturbation and increase the spectral density near the peak frequency. This might be closely related to self-stabilization of spectral form. On the other hand, when the ratio between the two peak frequencies is large, as indicated in Fig. 2d, positive and negative peak values appear near the high-frequency peak, which represents a downshift of that peak.

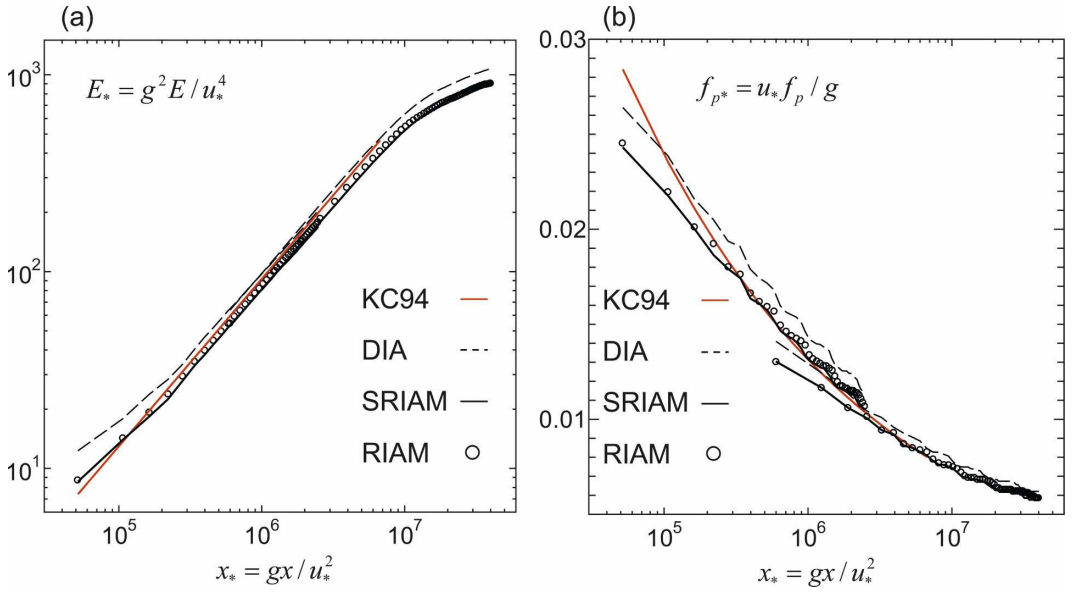

FIG. 3. (a) Nondimensional energy $E_* = g^2E/u_*^4$ and (b) nondimensional peak frequency $f_{p*} = u_*f_p/g$ as a function of nondimensional fetch $x_* = gx/u_*^2$, where u_* is wind friction velocity and g is gravitational acceleration.

d. Fetch-limited wave growth

To investigate the applicability of the methods in a more practical setting, all three methods were compared in the case of fetch-limited wave growth and with the observational results of Kahma and Calkoen (1994). We considered a one-dimensional domain with a depth of 5000 m. The models were run with uniform and steady wind fields. The wind speed at a height of 10 m (U_{10}) was set to 20 m s^{-1}. To investigate the effects of spatial resolution, test runs were performed for both short-fetch (2°) and long-fetch (30°) runs with different resolutions, following the method of Tolman and Chalikov (1996). Spatial resolution was set to 0.05° and 0.5° for the short- and long-fetch runs, respectively. A first-order upwind scheme was applied for wave propagation.

Figures 3a,b show nondimensional energy and nondimensional peak frequency, respectively, as a function of nondimensional fetch. All variables were nondimensionalized using friction velocity u_* and gravitational acceleration g. Time integration was performed until the spectrum seemed nearly saturated (t = 96 h).

The results of SRIAM and RIAM were in good agreement, whereas DIA had somewhat larger values. The profile of Kahma and Calkoen (1994) shown in the figure indicates the intermediate value for each result. There were small biases for each result; however, all results showed reasonable agreement in spatial pattern for nondimensional fetch. This is consistent with the findings of Hasselmann et al. (1985), who reported that DIA represented parameters such as wave energy and peak frequency well when using other sets of wind input (Snyder et al. 1981) and dissipation (Komen et al. 1984).

However, there were significant differences among the computed spectral shapes, especially those computed by DIA. Figure 4 shows the frequency and directional wave spectral energy densities at nondimensional fetch $x_* = 1.88 \times 10^6$. The spectral shape calculated by SRIAM was slightly broader in frequency and narrower in directional density than that calculated by RIAM. The two-dimensional distribution of the wave spectrum calculated by DIA was much broader than that by RIAM. Moreover, bimodal distribution appeared on the low-frequency side of the peak frequency. That is, DIA redistributed wave energy at much larger oblique angles than estimated by exact nonlinear transfer, which is a recognized shortcoming of DIA (Komatsu and Masuda 1996; Van Vledder 2006).

3. Impact of nonlinear energy transfer on wave–current interactions

Holthuijsen and Tolman (1991) performed a detailed investigation on the effect of the Gulf Stream on ocean waves under both swell and storm conditions. The simulations were performed using DIA for Snl. They found that the Gulf Stream significantly affected not only the wave height but also the shape of the wave spectra, via wave refraction. They also found that under

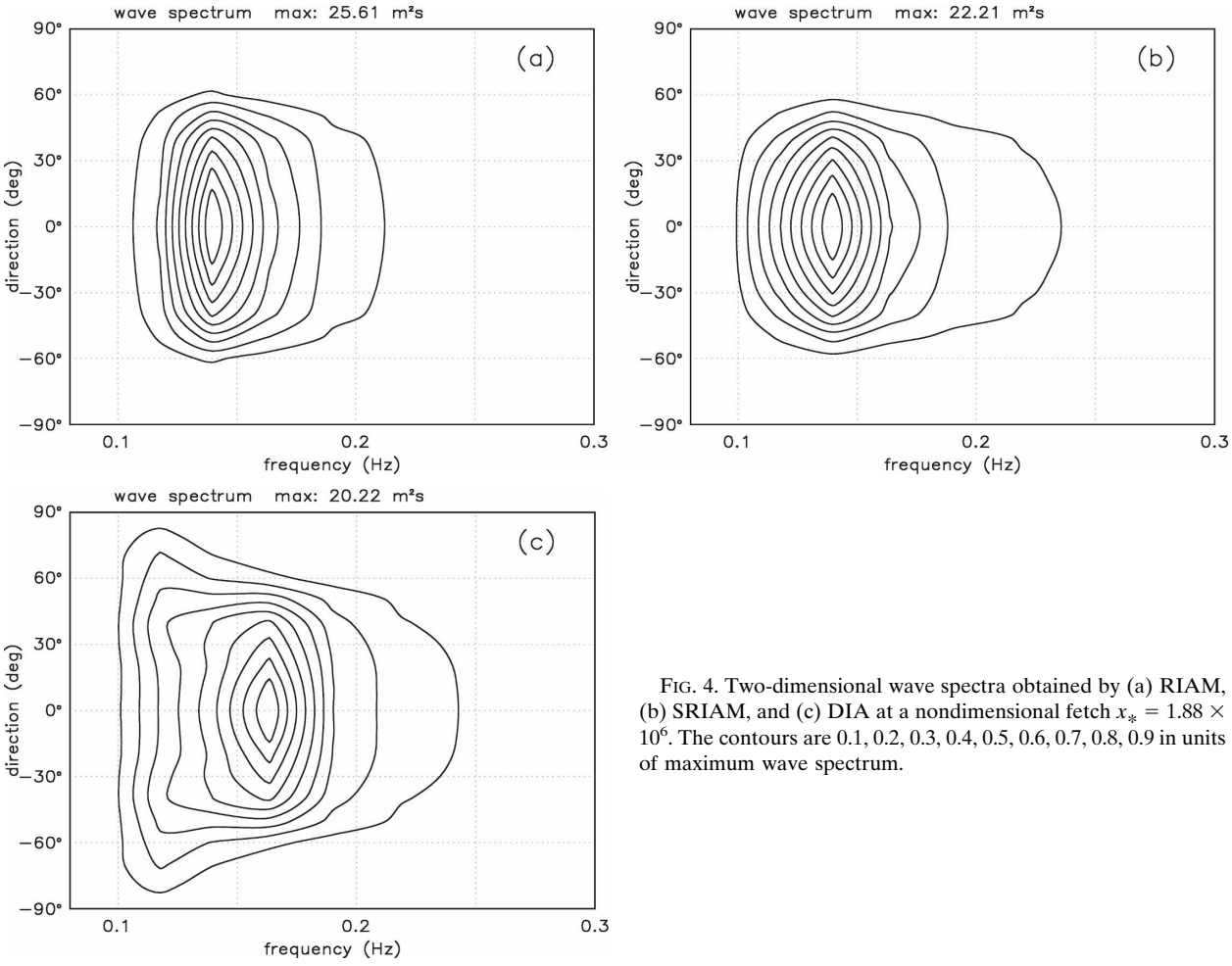

FIG. 4. Two-dimensional wave spectra obtained by (a) RIAM, (b) SRIAM, and (c) DIA at a nondimensional fetch $x_* = 1.88 \times 10^6$. The contours are 0.1, 0.2, 0.3, 0.4, 0.5, 0.6, 0.7, 0.8, 0.9 in units of maximum wave spectrum.

storm conditions, the physical processes of generation, dissipation, and wave–wave interactions were considerably enhanced in the countercurrent region. Their results highlighted the importance of wave–current interaction for wave forecasting and hindcasting. However, because the DIA only poorly approximates Snl, they did not assess its role in their study. Instead, they gave a heuristic estimate of the intensity of the physical processes, which they calculated from the integrals of the source functions over the frequency-directional domain.

Following the studies just described, we performed two numerical simulations of ideal current fields using SRIAM to investigate the effects of nonlinear transfer on wave–current interactions. We began with a simulation that involved wave propagation against a shear current with and without the transfer function to examine the effects of nonlinearity. To investigate variation in spectral shape in relation to current, we also performed a numerical simulation of wind–sea propagation through a current ring with wind input and white capping.

a. Wave propagation against a shear current

To demonstrate the effects of the Snl on wave–current interactions, we conducted numerical simulations of wave refraction and strain by horizontal shear currents without wind input and dissipation. Four numerical simulations were performed: the linear case without Snl and three nonlinear cases with Snl calculated by SRIAM, RIAM, and DIA. The accuracies of DIA and SRIAM were examined against RIAM, as described in the previous section. We used a model domain of $10° \times 10°$ with a spatial resolution of 0.2° and 0.25° (51×41 grid points) covering 180°–190°E, 5°S–5°N to clarify the wave refraction by reducing the wave propagation along the great circle. The incident wave spectrum (JONSWAP spectrum with significant wave height of 1.2 m, peak frequency of 0.2 Hz, and $\cos^4\theta$ directional spreading) was set to propagate against an

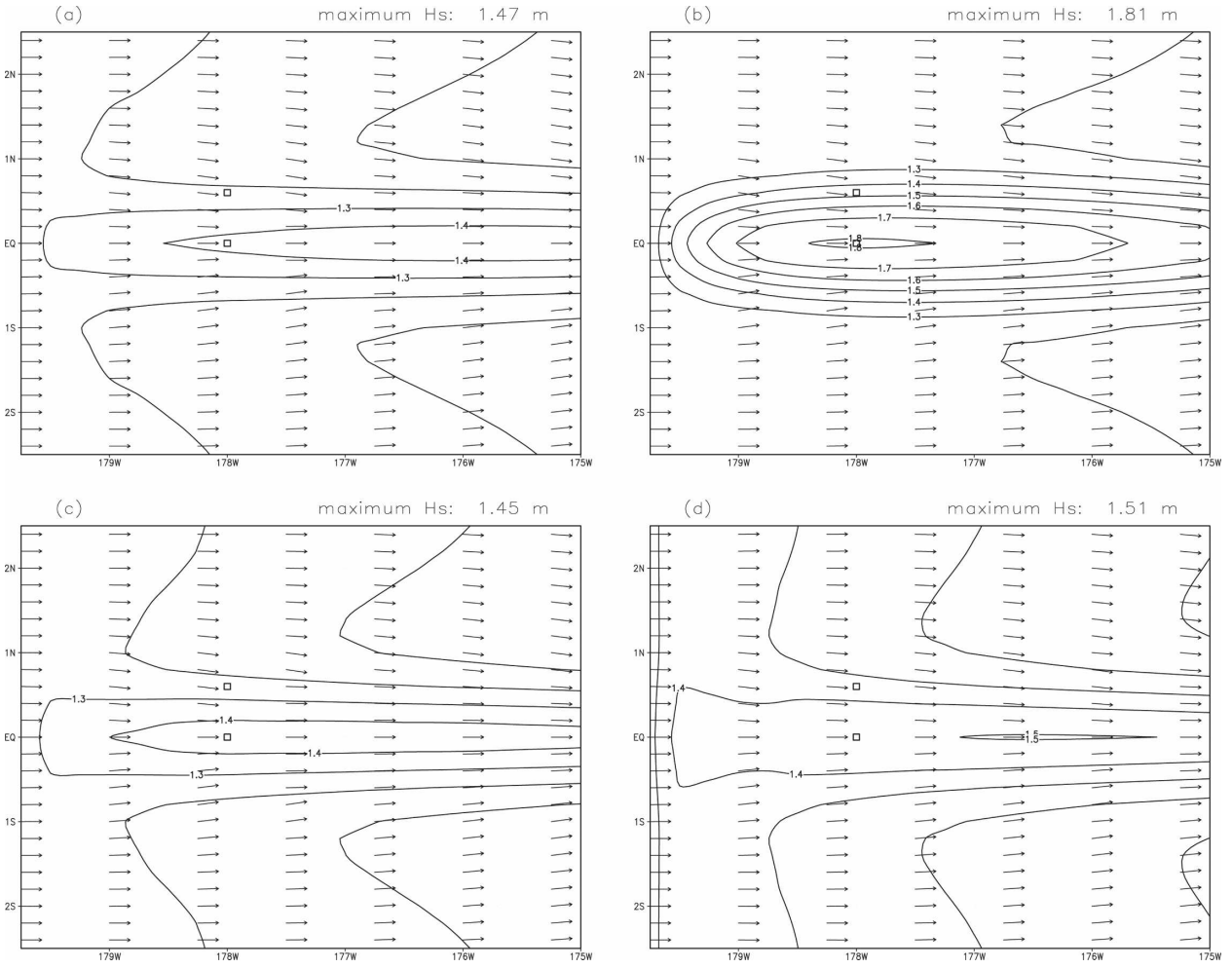

FIG. 5. Spatial distribution of the significant wave height (contours) and peak direction (arrows) obtained by (a) RIAM, (b) linear computation, (c) SRIAM, and (d) DIA around the core of the jet after 96 h of time integration.

ocean current at the western boundary. Along the northern and southern boundaries, the gradient of the wave spectrum normal to the boundary was set to zero. Wave energy was set to zero along the eastern boundary. Initial wave spectra in the domain were assumed to be zero. The current velocity was given as a 1D Gaussian profile:

$$U(y) = U_0 \exp[-(y/y_w)^2], \tag{4.1}$$

where U_0 is the peak current velocity (1.5 m s^{-1}), y is latitude, and y_w is 0.7°.

Figure 5 shows the spatial distribution of the significant wave height and peak direction after 96 h of time integration. In all cases, significant wave height was concentrated along the core of the jet, because of wave refraction and strain by the shear current. However, there were clear differences. First, the effects of refraction and strain were more apparent in the linear computations than in the nonlinear computation. The maximum significant wave height exceeded 1.8 m in the linear computations, corresponding to a 50% increase in incident wave height. On the other hand, it was less than about 1.5 m in the nonlinear computation, indicating that current-induced modulation of significant wave height was diminished in this calculation. Second, the spatial distribution of the significant wave height in SRIAM showed almost the same pattern and magnitude as in RIAM. This implies that SRIAM can reproduce the Snl of the RIAM method, whereas DIA cannot. Differences in significant wave heights are closely linked to wave spectral properties. To evaluate these differences in detail, we investigated the wave spectra and associated Snls at two locations: 0°, 182°E and 0.6°, 182°E (black squares in Fig. 5).

Figure 6 compares the wave spectra and Snls at the center of the countercurrent (0°, 182°E) for the linear

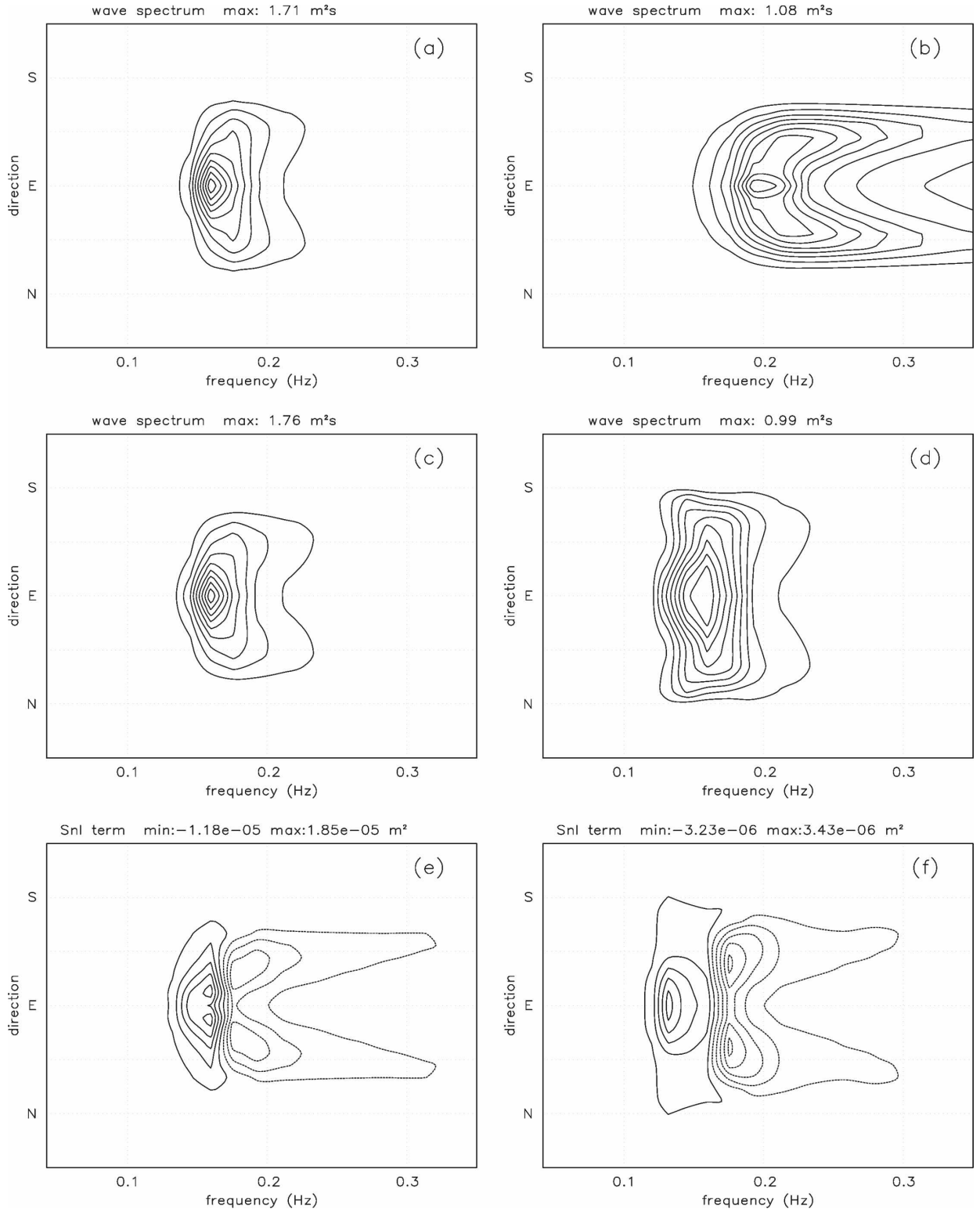

FIG. 6. (a)–(d) Wave spectra and (e)–(f) nonlinear transfer functions at the center of the countercurrent (0°, 182°E): wave spectra obtained by (a) RIAM, (b) linear computation, (c) SRIAM, (d) DIA, and the nonlinear transfer functions obtained by (e) SRIAM and (f) DIA. The contour interval (CI) of wave spectra is 0.1 in units of maximum wave spectrum. The CI for the transfer function are ±(0.1, 0.3 0.5, 0.7, 0.9) in units of maximum absolute value. Solid (dashed) lines represent positive (negative) values.

and nonlinear computations. SRIAM (Fig. 6c) successfully reproduced the wave spectrum calculated by RIAM (Fig. 6a). The spectral shapes estimated by RIAM and SRIAM at this position were much narrower in frequency and directional space than in the DIA result (Fig. 6d) or linear calculation (Fig. 6b). The wave spectrum was sharply peaked in the original direction of the incident wave (i.e., eastward), yet there was a downshift in peak frequency (Figs. 6a,c). In contrast, the linear case produced three peaks in different directions, presumably due to ray focusing or the formation of wave caustics (Fig. 6b), resulting in a broad directional distribution. Moreover, the shear currents broadened the frequency distribution at high frequencies, while the peak frequency remained constant (= 0.2 Hz), that is, did not downshift.

The difference between the nonlinear and linear wave evolutions can be explained by reviewing the results of the nonlinear transfer of energy calculated by SRIAM (Fig. 6e). High-frequency energy (0.18–0.22 Hz) that was refracted northeast and southeast was transferred to the low-frequency spectrum (0.14–0.17 Hz) in its original eastward direction. That is, the Snl concentrated the spectral components associated with wave refraction toward the original direction of the incident wave.

In DIA (Fig. 6d), peak frequency, direction, and total spectral energy (thus significant wave height) were consistent with those of RIAM and SRIAM. However, frequency and directional bandwidth were extremely broad, and spectral shape was clearly distorted compared to those of RIAM and SRIAM. For example, there was a trimodal directional distribution around the lower-frequency region (~0.14 Hz). The Snl calculated by DIA (Fig. 6f) transferred the refracted wave components to the low-frequency region in an eastward direction, similar to SRIAM. However, DIA broadened the wave spectrum, a typical shortcoming of the method, as mentioned above.

Figure 7 shows the spectrum and Snl where the horizontal shear of the current reached its maximal value (0.6°N, 182°E). Again, the wave spectral shapes calculated by SRIAM and RIAM were identical (Figs. 7a,c). On the other hand, the spectral shape calculated by DIA (Fig. 7d) was clearly different due to the method's limited applicability to complex wave fields. These results demonstrate that it is unreasonable to argue about spectral shape when DIA is used as the transfer function. Therefore, hereafter we discuss the results of SRIAM only.

Linear refraction veered the wave spectral peak toward the east-southeast (Fig. 7b), whereas when nonlinear transfer was considered, the spectral peak broadened in the southeast to east directions (Figs. 7a,c). In addition, this coincided with a distinct downshift in peak frequency. The Snl (Fig. 7e) indicated that energy was transferred from high frequency (0.18–0.22 Hz) with an east-southeast direction to low frequency (0.14–0.16 Hz) with an eastward direction. Again, the Snl attempted to retain spectral form by reducing refracted wave components and increasing the wave spectrum in the direction of the incident wave. These results strongly suggest that current-induced modulation in the direction of the wave spectrum is weakened via the self-stabilization effect of the Snl. As a result, concentration of the wave energy around the countercurrent due to linear focusing is weakened, and the energy is defocused.

Hubbert and Wolf (1991) investigated the wave spectrum deformation of a circular current eddy and found a considerable broadening of the directional distribution of the wave spectra; no downshift in peak frequency was apparent because they neglected the nonlinear term. Our linear calculation qualitatively agrees with their results. However, our nonlinear-based results indicate a different pattern of spectral deformation because of the downshift in spectral peak frequency and self-stabilization of the spectral form, especially the directional spreading.

b. Wind–wave evolution in a circular eddy current

We conducted a numerical simulation of the evolution of a wind-generated wave in a circular current ring. We used SRIAM as the nonlinear source function to improve the results.

The computational domain was $10° \times 6°$ with a spatial resolution of 0.1° and 101×61 grid elements. A steady and homogeneous wind field was assumed. Wind speed, U_{10}, and direction were set at 10 m s^{-1} and eastward, respectively. To consider the local effects of current on wave generation, the fetch effect was removed by setting the gradient of the wave spectrum to zero along the northern, southern, and western boundaries. A low level of wave action density was added to the seeding frequency instead of providing an initial wave spectrum a priori to accelerate the initial wave spectrum growth (Tolman 2002).

The current field that we investigated followed that of Mathiesen (1987) and Hubbert and Wolf (1991), that is, a counterclockwise-turning ring of varying current speeds and radii. The tangential current velocity profile $U(r)$ was given as

$$U(r) = U_1 r/r_1 \quad r \le r_1,$$
$$U(r) = U_0 \exp\{-[(r - r_0)/br_0]^2\} r > r_1, \qquad (4.2)$$

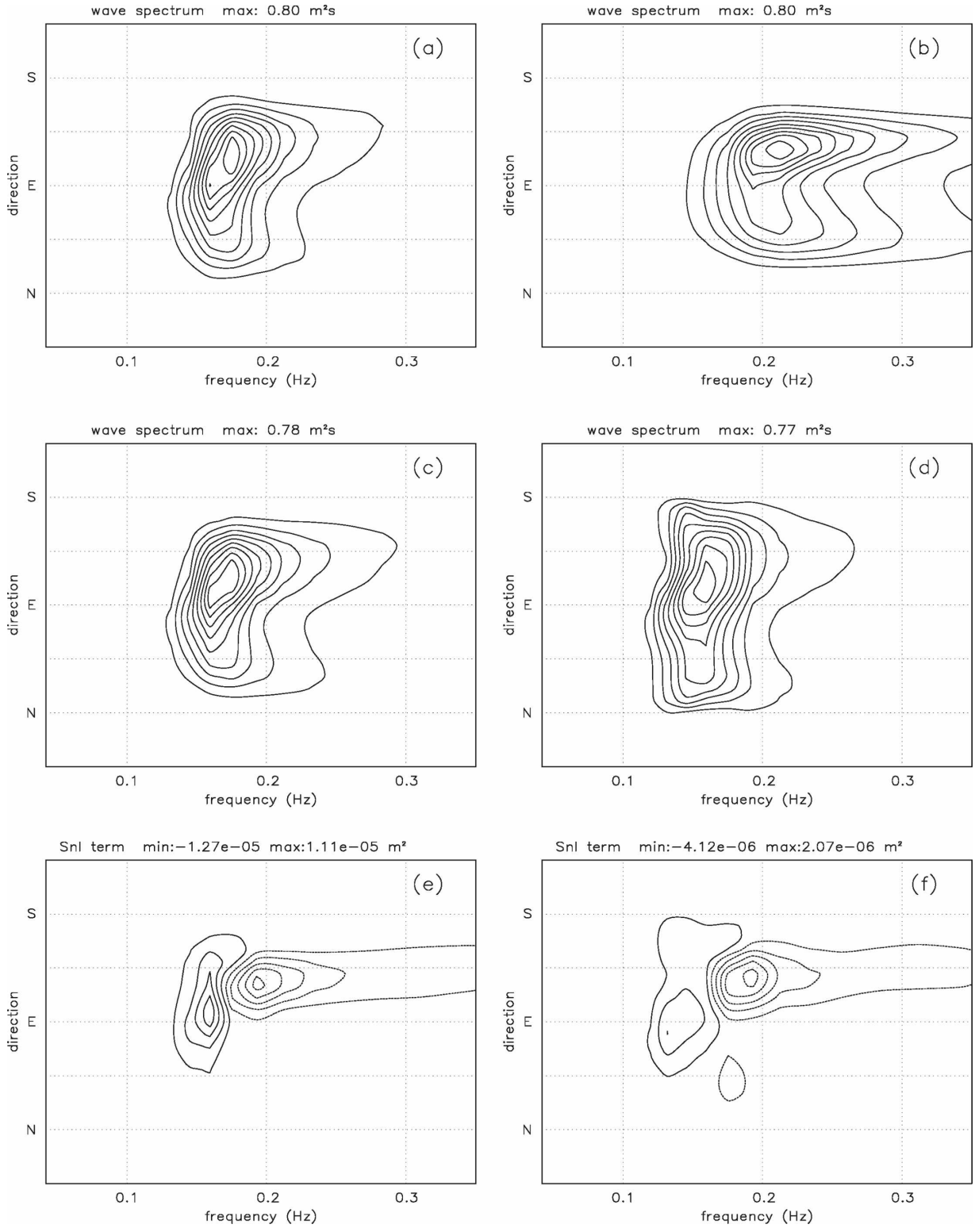

FIG. 7. Same as Fig. 6, but where the horizontal shear of the current becomes a maximal value (0.6°N, 182°E).

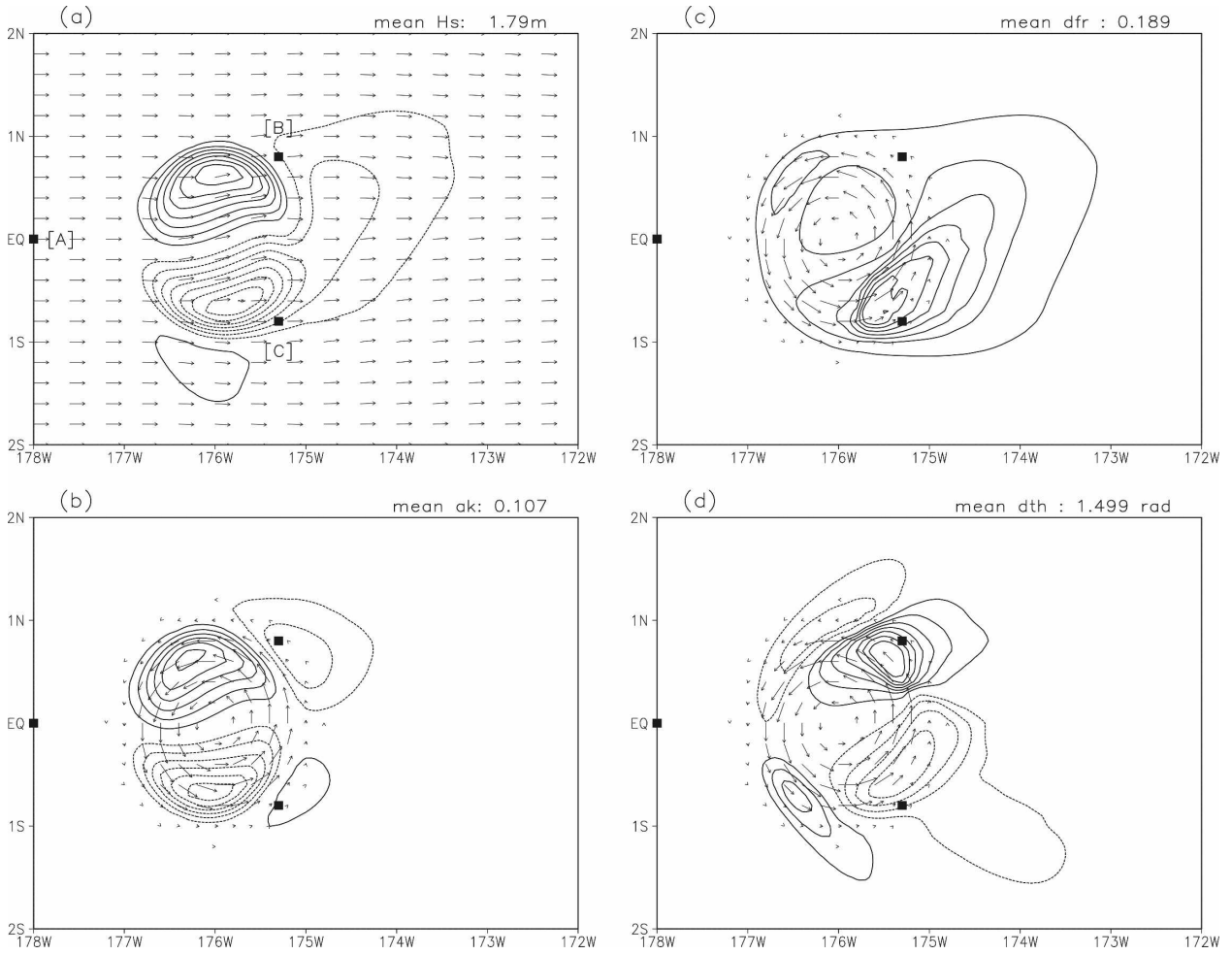

FIG. 8. Spatial distribution of wave characteristics around the turning ring: (a) significant wave height (CI: 0.05 m) and peak direction (arrows); (b) mean wave steepness (CI: 0.004) defined by $0.5\ H_s \times k_m$, where H_s is significant wave height and k_m is mean wavenumber estimated from the spectral average of the wavenumber; (c) frequency bandwidth parameter (CI: 0.05) defined by Eq. (4.5); and (d) directional bandwidth parameter (CI: 0.1 rad) defined by Eq. (4.6). Solid (dashed) lines represent positive (negative) values obtained by subtracting mean values.

where

$$r_1 = 0.5r_0[1 + (1 - 2b^2)^{0.5}],$$
$$U_1 = U_0 \exp\{-[(r_1 - r_0)/br_0]^2\}, \quad (4.3)$$

and $b = 0.3$ and the maximum current velocity U_0 is 1.5 m s^{-1} at a radius of $r_0 = 0.7°$ from the center of the eddy (arrows in Figs. 8b–d). To investigate the spatial distribution of current effects on the wave spectrum, we defined two parameters to characterize frequency and directional bandwidth. These were defined as the difference between the frequency and the directional angle, where the energy is half the maximum:

$$df = (f_2 - f_1)/f_p, \quad F(f_1) = \mathrm{F}(f_2) = 0.5F_{\max}, \quad (4.4)$$

$$d\theta = \theta_2 - \theta_1, \quad F(\theta_1) = F(\theta_2) = 0.5F_{\max}, \quad (4.5)$$

where f_p is peak frequency, $F(f)$ is the one-dimensional spectrum for frequency, $F(\theta)$ is the one-dimensional spectrum for direction, and $F_{\max}$ is the maximum value of the wave spectrum. The spectral bandwidths of frequency and direction are instrumental in altering wave-height probability density from the Rayleigh distribution (Janssen 2003; Onorato et al. 2004; Waseda et al. 2009). These parameters are relevant for identifying seas with a high chance of producing a freak wave.

Figures 8a–d show the spatial distribution of significant wave height and peak direction, mean wave steepness, frequency bandwidth, and directional bandwidth after 36-h integration, respectively. The wave age, defined as the phase velocity of the peak frequency divided by U_{10}, is about 1 for the entire domain. The sea state is fully developed and corresponds to an old wind

sea. To isolate the current effect, mean values obtained by averaging the upwind region (180°–184°E) were subtracted from each value. The refraction and strain effects of the current modulated the spatial distribution of these parameters around the current ring. Significant wave height increased in the countercurrent region and decreased in the following current region, mostly confined to the eddy. This phenomenon has been described by Holthuijsen and Tolman (1991). The variation in significant wave height reached 20% of the average significant wave height. The spatial distribution of wave steepness was almost the same as that of significant wave height. The positions of positive and negative peaks of wave energy and steepness anomalies closely corresponded to maximum current speed with opposing directions. On the other hand, the opposite occurred because of the asymmetric pattern of the ring across the mean wave direction.

On the other hand, the spatial distribution of the spectral bandwidths showed a completely different pattern. The current broadened the frequency bandwidth around the eddy, especially just beyond the region with the maximum following current. Moreover, the distribution of negative and positive effects was not symmetric, as it was for significant wave height (Fig. 8a). For directional bandwidth, positive and negative peak values appeared beyond the following and countercurrent regions, respectively. This distribution was almost symmetric to wind direction, but the positions of the peak values differed from those of significant wave height and wave steepness. The spatial distribution of these parameters implies that freak waves due to current rings do not occur under these particular conditions; however, as this implication is outside the scope of this study, further studies are necessary to confirm this possibility.

Figure 9 shows frequency-directional spectra and associated Snls at points A (0°, 182°E), B (0.8°N, 184.7°E), and C (0.8°S, 184.7°E) indicated in Fig. 8. Point A is a reference position of the free-of-current effect. The total energy at the three points was almost identical (Fig. 8a). Point B represents the position where the countercurrent broadened the directional bandwidth. Wave spectral energy was produced mainly in the eastward direction due to the wind input (not shown here) corresponding to wind direction. However, the peak spectrum did not appear in the eastward direction, and the directional distribution became bimodal around the peak frequency in the northeast and east-southeast directions. This was due to current refraction and strain in the countercurrent region. In contrast, the main role of the Snl was to redistribute wave energy from higher frequencies (0.2–0.35 Hz) in the east-southeast to lower frequencies (0.12–0.15 Hz) in the eastward direction. That is, nonlinear transfer modified the directionally broadened spectral energy, concentrating it toward the original direction (i.e., eastward). At the same time, the Snl downshifted the spectral peak. Position C represents the position where spectral bandwidth was broadened in frequency and narrowed in direction. Directional bandwidth was narrowed by the following current, and the peak direction was nearly due east. In addition, the high-frequency region ($f > f_p = 0.16$ Hz) had a large part of the total energy compared to the wave spectrum at points A and B, and the frequency bandwidth was broad. There were two positive peak values for the Snl around peak frequencies in the east-southeast and east-northeast directions. There was a negative peak value around the high-frequency region (0.2–0.25 Hz) with a nearly due-east direction. That is, the Snl moved the high-frequency component in the eastward direction, broadening the directional spreading around the peak frequency.

Our results indicate that the Snl reduces spectral shape variation, especially in the directional domain induced by the current, and thus wave spectral components with different directions veer toward the original direction. Moreover, for wave spectra with broader or narrower directional spreading, the Snl has the opposite effect.

4. Hindcast simulation

A few studies have demonstrated the significance of wave–current interactions for operational wave modeling from global or regional perspectives (Janssen et al. 2005; Wolf 2003; Komen et al. 1994). The Snl is crucial for estimating wave characteristics and spectral shape, as shown in the previous sections; however, DIA has been used for almost all operational wave modeling to date, despite its inaccurate approximations. In this section, we focus on the influence of ocean currents on waves around the strong jet of the Kuroshio, using wind and current reanalysis data. To obtain more accurate results and investigate the role of nonlinear transfer in wave–current interactions, we used SRIAM as the transfer function.

A hindcast simulation was performed over a 1-month integration period (October 2004). This was an unusual month in that three consecutive typhoons (T0422, T0423, and T0424) struck Japan, causing enormous damage and casualties both on the coast and inland, especially associated with typhoon 0423 (nicknamed Tokage). In addition, during this period, the Kuroshio had a large meandering path for the first time in about 15 yr; the main axis of the current separated from the

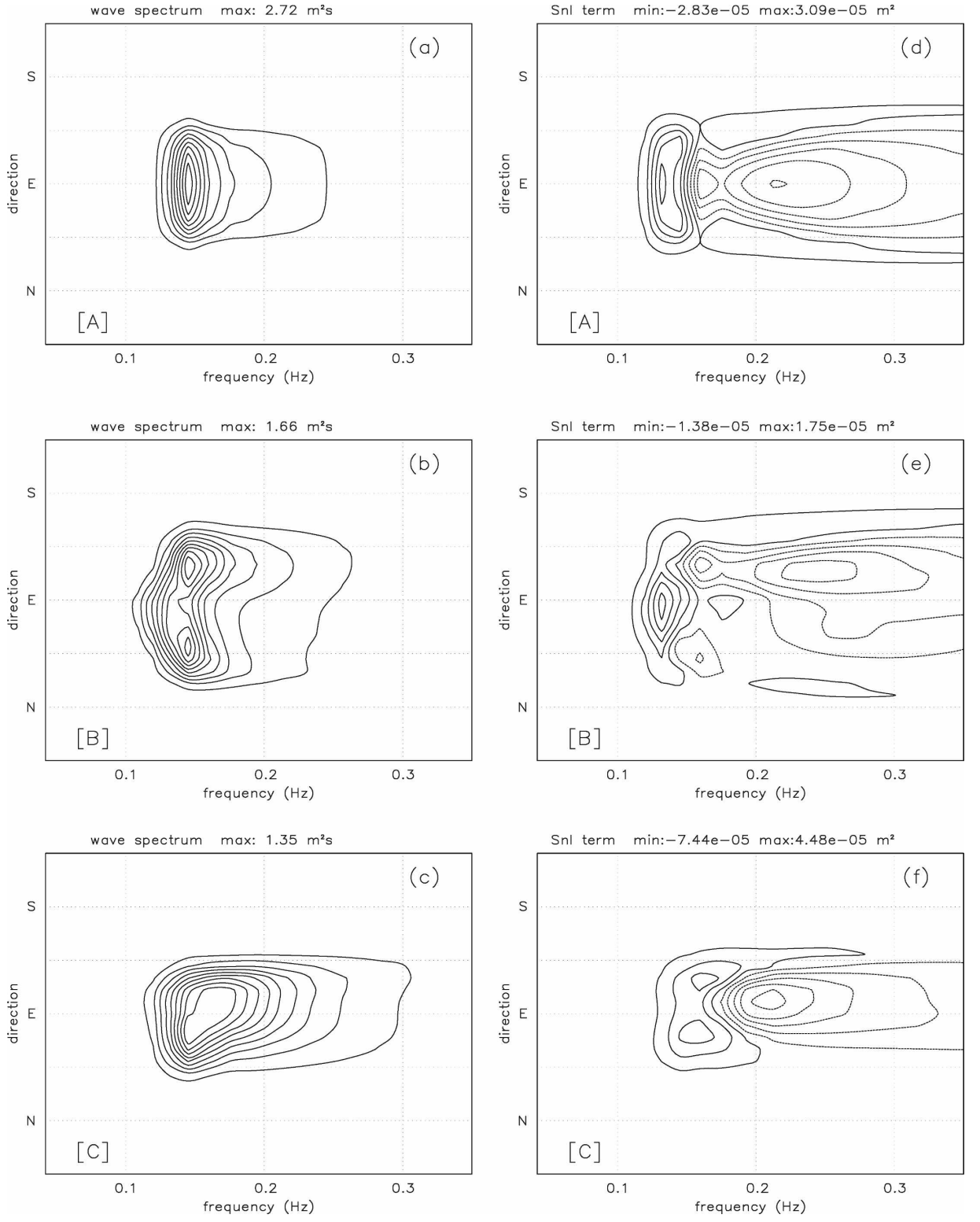

FIG. 9. (a)–(c) Wave spectra and (d)–(f) nonlinear transfer functions at the labeled locations shown in Fig. 8: The CI for the wave spectra is 0.1 in units of maximum wave spectrum and for the transfer function is 0.2 in units of maximum absolute value. Solid (dashed) lines represent positive (negative) values.

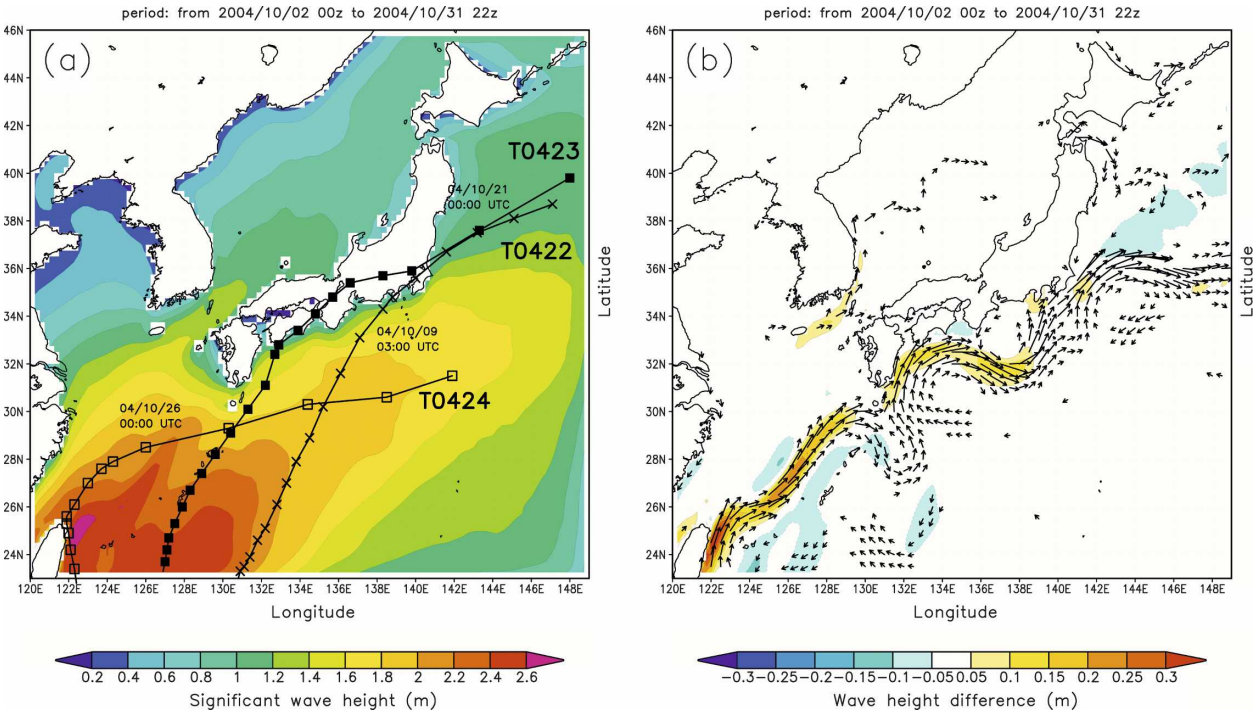

FIG. 10. (a) Average monthly spatial distribution of significant wave height with ocean current coupling. The three typhoon paths (T0422, T0423, and T0424) are indicated as black lines with ×, ■, □, respectively. Markers are plotted every 3 h. (b) Averaged wave height difference between simulations with and without current data. Arrows represent current vectors having speeds greater than 20 cm s^{-1}.

coast off the Kii Peninsula (33.4°N, 135.8°E) and from there ran southeastward.

The wind field was described using the Grid Point Value of the Mesoscale Model (GPV-MSM, 1/8°–1/10° resolution) distributed by the Japan Meteorological Agency. This reanalysis dataset is widely used for regional numerical wave simulations around Japan. However, as we discussed in the introduction, accurate evaluation of the current field is also an important factor. We used current field data from the Japan Coastal Ocean Predictability Experiment (JCOPE) model developed at the Frontier Research Center for Global Change (Guo et al. 2003; Miyazawa et al. 2005; Kagimoto et al. 2008). JCOPE is based on the Princeton Ocean Model (POM), a high-resolution regional model (12°–62°N, 117°E–180°, at 1/12° resolution) that is embedded in a low-resolution basin-wide model (1/4° resolution) and assimilates sea surface height, temperature, and salinity from various sources. The model successfully simulated the appearance of a large meander of the Kuroshio in October 2004, as shown in Fig. 10b (Kagimoto et al. 2008).

The wave model was driven by 6-hourly wind stress estimates from GPV-MSM and a 2-day mean current field from the JCOPE reanalysis product linearly interpolated at every integration time interval between 1 October and 1 November 2004. The computational domain was set to 23°–46°N and 120°–149°E. The spatial resolution was 0.25° with 117 × 93 grid elements. A third-order accurate numerical scheme was used to describe wave propagation (Tolman 2002), and SRIAM was applied to evaluate the Snl. The simulation was performed with and without current data to investigate the impact of wave–current interactions.

Figure 10a shows the average monthly spatial distribution of the significant wave height with ocean current coupling, and Fig. 10b shows the difference in wave height with and without current data. The three typhoon paths are indicated in Fig. 10a as black lines. Mean significant wave height increased around the southwestern part of the domain, indicating that an intermittent and strong local wind field, such as a typhoon event, caused an intensification of significant wave height. Moreover, the differences in significant wave height over the entire Kuroshio were substantial, especially near the eastern coast of Taiwan. The largest differences were mainly along the Kuroshio axis, as shown in the numerical simulation for the current ring (Fig. 8a).

However, the wave–current interactions associated

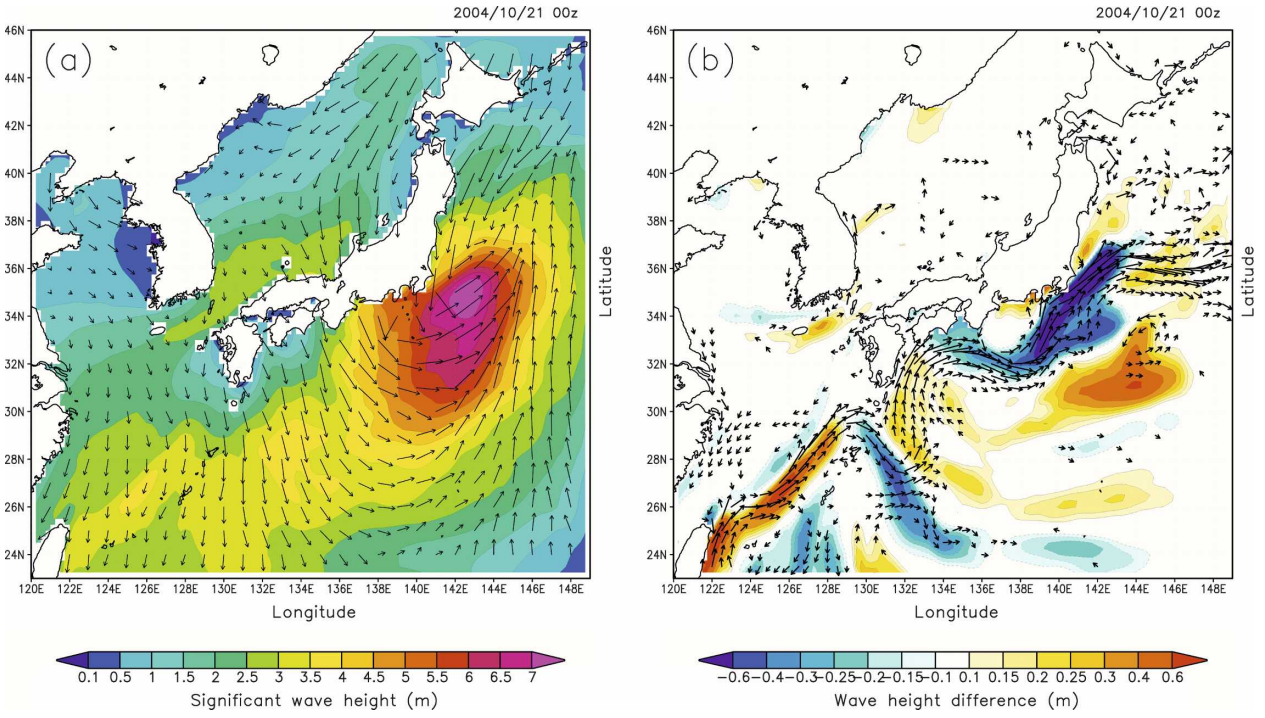

FIG. 11. (a) Instantaneous plane view of significant wave height (contours) and wind vectors (arrows), (b) wave height difference between simulations with and without current data (contours) and current vectors (arrows) when Typhoon Tokage passed Japan (at 0000 UTC 21 Oct 2004).

with the changes in surface wind and current seem rather complex. Figures 11a,b show an instantaneous plane view of the differences in significant wave height and between wave height with and without current data when Typhoon Tokage passed by Japan (at 0000 UTC 21 October 2004). The typhoon initially passed over the southern part of the Kuroshio main axis (Fig. 10) and then over the northern part of the axis (Figs. 10, 11). Corresponding to these relative positions between the typhoon and the main axis of the current, there was wave convergence in the countercurrent region and wave divergence in the following current region (Fig. 11b). Moreover, the differences in significant wave height extended for quite a distance away from the Kuroshio, downwind. The wave-height modulation induced by the current originated from both small and large meanders of the current around 29°N, 131°E and 32°N, 138°E, respectively. These results indicate that the effects of wave–current interactions are not only local but also extend to more distant areas. As demonstrated here, wave–current interactions are highly sensitive to small current structures, and therefore a realistic representation of the current field is very important for high-resolution wave forecasting.

Figure 12 shows an instantaneous plane view of the directional bandwidth parameter defined by Eq. (4.5) around the upstream region of the Kuroshio without and with current simulations (Figs. 12a,b, respectively) at 0000 UTC 21 October 2004. Black arrows and white arrows represent peak wave direction and current vectors, respectively. The spatial distributions of the directional bandwidth are completely different. While only a slight decrease in directional spreading occurred when current simulations were not included (Fig. 12a), spreading inside the current increased (Fig. 12b). To examine the effects of the current on spectral shape modulation in greater detail, we considered the wave spectrum and Snl inside the current (26.8°N, 125.7°E; black square Fig. 12) again without and with current simulations. As shown in Figs. 11b, 12, the properties of the wave were significantly modulated and appeared in the differences of spectral shape. One obvious effect was that without current data, there was a quasi-unidirectional wave spectrum in the south-southwestern direction (Fig. 13a), whereas when current data were included there were two spectral peaks with different directions (south and southwest) (Fig. 13b). After Typhoon Tokage passed over this area, the wave field (without current) was dominated by swells traveling in south to southwestern directions, and the wave field was almost homogeneous spatially, as seen in Fig. 12a. However, swells were trapped along the Kuroshio

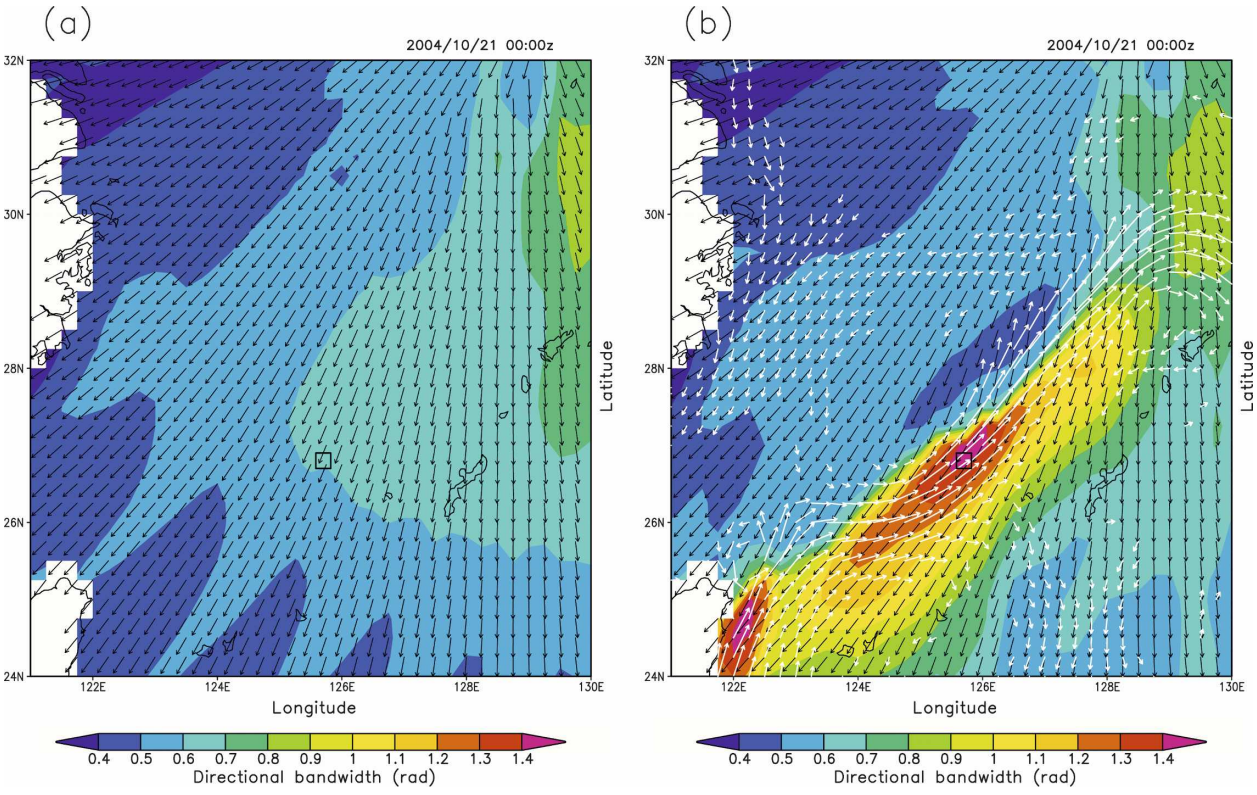

FIG. 12. Spatial distribution of the directional bandwidth parameter defined by Eq. (4.5) around the upstream region of the Kuroshio in simulations (a) without and (b) with current data (0000 UTC 21 Oct 2004). (a), (b) Black arrows represent peak wave directions. (b) White arrows represent current vectors. Black squares indicate the locations of the wave spectra and transfer functions shown in Fig. 13.

and traveled upstream against the current (southwest). In addition, swells entering the current from the northeast refracted locally, shifting incoming swell energy southward. This created a second peak in the spectrum, increasing directional spreading, as indicated in Fig. 12b. The convergence of swells due to these wave–current interactions concentrated wave energy within the current (Fig. 11). Again, the differences in wave characteristics and spectral shape over the Kuroshio were substantial.

Furthermore, the Snl again had some interesting effects on directionality (Figs. 13c,d). Without current data, two positive peak values of the Snl appeared (south and southwest), and a negative peak value appeared in the south-southwest around the peak frequency (0.08–0.1 Hz), as shown in Fig. 13c. These patterns suggest that nonlinear transfer broadened the directional spreading of swells traveling at this point. In contrast, as confirmed in the numerical simulation that included current data (Fig. 13d), nonlinear transfer narrowed the directional spreading of broadened wave spectra. This is similar to the effects of the Snl on frequency and directional space (Fig. 6e). In addition, positive peak values of the transfer function appeared around 0.09 Hz (south-southwest direction) corresponding to the spectral peak in the simulation without current data (Fig. 13a), retaining spectral shape without modulation due to current effects. These results indicate that self-stabilization, especially for current-modulated wave direction, is an important mechanism of the Snl in simulations based on actual ocean current and wind data.

One of the central aims of this study was to investigate the impact of Snl on the wave field. We were particularly interested in answering the long-standing question as to how Snl alters the wave statistics and the shape of spectra in realistic situations. To address this, we investigated the effects of the nonlinear transfer source term accuracy on the results of a hindcast simulation using SRIAM and DIA. The probability density function of (i) significant wave height, (ii) peak frequency, (iii) frequency bandwidth, and (iv) directional bandwidth calculated by SRIAM (-) and DIA (o) are shown in Fig. 14. We analyzed the data using a 1-month integration period. As shown in Figs. 14a,b, SRIAM and DIA were in reasonable agreement for the signif-

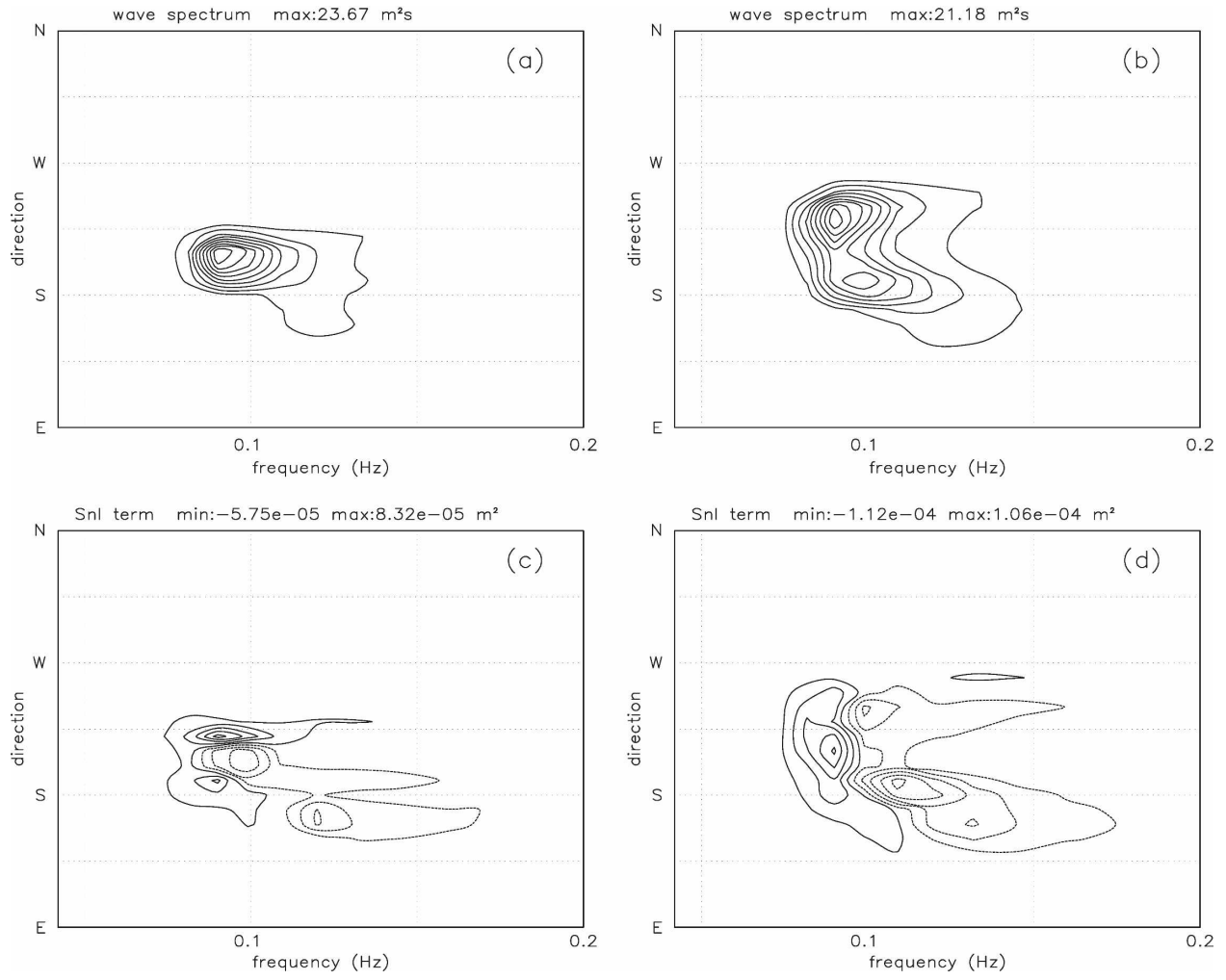

FIG. 13. (a), (b) Wave spectra and (c), (d) nonlinear transfer functions inside the Kuroshio (26.8°N, 125.7°E; black square in Fig. 12) for simulations without and with current data. The CI for wave spectra is 0.1 in units of maximum wave spectrum and for transfer function is 0.2 in units of maximum absolute value. Solid (dashed) lines represent positive (negative) values.

icant wave height and the peak frequency. However, large differences were observed in the frequency and directional bandwidth results, which implied large differences in the shapes of the spectra. These results were consistent with the previous results for fetch-limited wave growth (see section 2d) and current-induced wave modulation (see section 3a). As we used the same wave input and dissipation source functions in both cases, the difference could only be due to the Snl terms. Because the four-wave resonant interaction redistributes wave energy inside the frequency-directional domain, it has an important role in determining the spectral shape. Our results suggested that when only statistical wave information is required, such as the significant wave height or peak period, the careful numerical evaluation of Snl is not necessary. However, when more detailed information is required, such as the spectral shape of the waves, Snl plays an important role. As mentioned previously, recent studies have suggested that the probability of freak wave occurrence is strongly related to the wave spectral shape, steepness, frequency, and directional bandwidth. Therefore, the accuracy of freak-wave predictions may depend on the Snl approximation used.

5. Conclusions

Despite numerous studies on the current-induced modulation of wave properties, few have attempted to investigate changes in spectral shape. To better understand the current-induced modulation of ocean wave spectral properties, and the role of nonlinear transfer in wave–current interactions, we implemented SRIAM to numerically evaluate nonlinear transfer and improve

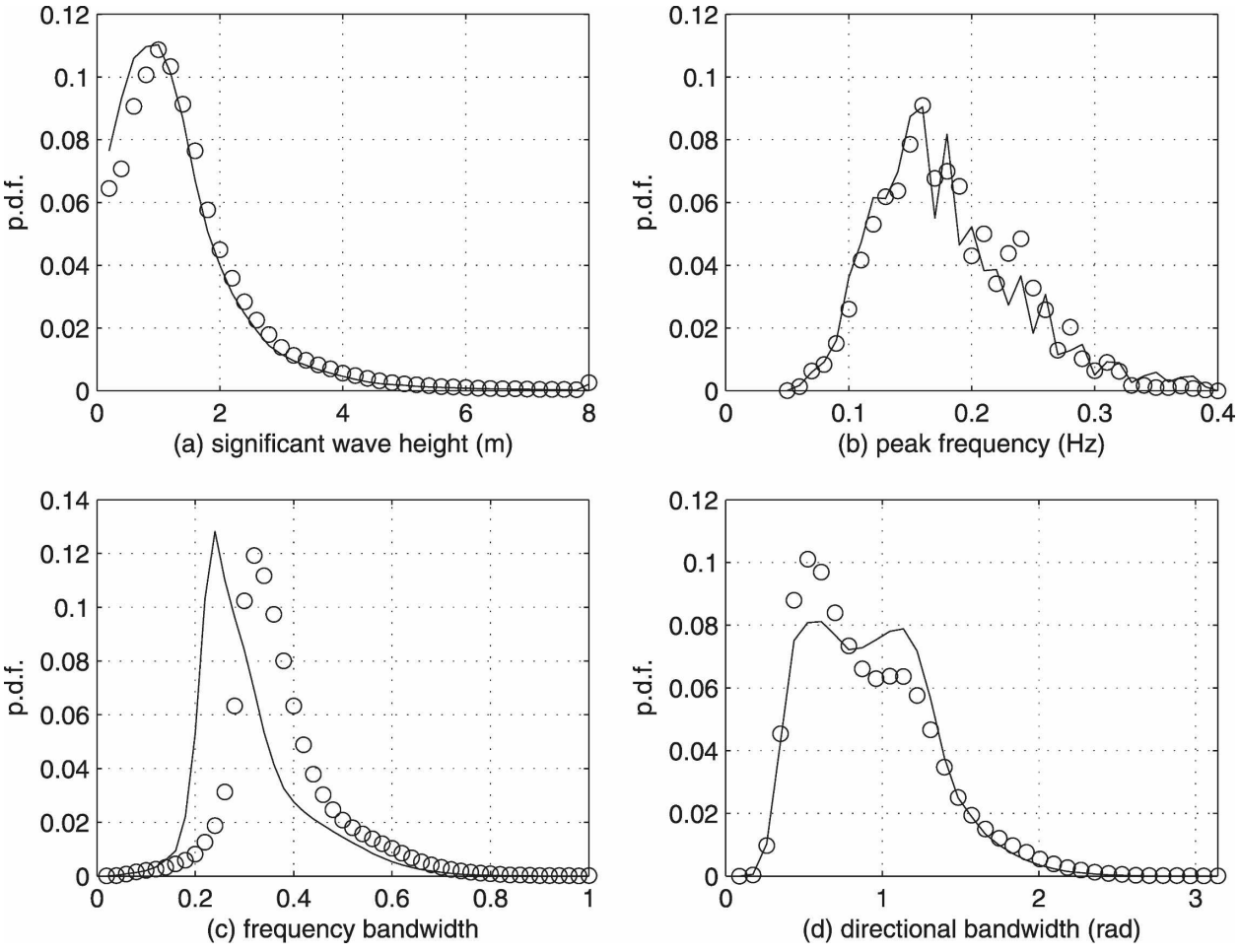

FIG. 14. Probability density function of (a) the significant wave height, (b) the peak frequency, (c) the frequency bandwidth, and (d) the directional bandwidth calculated using SRIAM (-) and DIA (o). Data over a 1-month integration period were analyzed.

spectral resolution with relatively low computational cost.

We investigated the performance of SRIAM for fetch-limited wave growth and spectral modulation by a jet current of selected wave spectra. The wave spectra and Snl calculated by SRIAM agreed well with those estimated by the rigorous RIAM method, whereas the DIA method was significantly less useful.

Our results indicate that refraction and strain are apparent in linear calculations but less so in nonlinear calculations. Because of the self-stabilization effect of the Snl, spectral form is retained, which redistributes the refracted wave energy. Consequently, significant wave height in the focal region is reduced. This interesting effect of nonlinear transfer was also found in simulations of the evolution of wind-generated waves propagating over a Rankin-type eddy current. As wave spectra tend to broaden and narrow due to refraction and strain by circular currents, the Snl induces an opposing force to this directional spreading. Again, the directional spectrum is self-stabilized due to nonlinear wave–wave interactions.

The hindcast simulation indicated that the difference in the average monthly significant wave height with and without current data was mainly constrained along the Kuroshio axis. However, the instantaneous difference in significant wave height extended for quite a distance away from the current downwind, suggesting that the effects of wave–current interactions are not only local but also extend to more distant areas. Spectral shape was also modulated by the Kuroshio. The spatial distribution of the directional bandwidth characterizing the spectral shape was completely different with or without current data, and the difference was substantial near the Kuroshio. In addition, the structure of the Snl denoted the self-stabilization effect, especially in changing the wave direction modulated by the current. Therefore, the important mechanism of nonlinear

transfer in self-stabilizing the spectrum and moderating the linear effect of wave refraction and energy focus was apparent based on real oceanic data. The hindcast simulation also demonstrated that while SRIAM and DIA show reasonable agreement for the significant wave height and the peak frequency, large differences were evident in the frequency and directional bandwidth values.

Further improvements are required before our modeling effort can be extended to practical and operational applications. In particular, the calculation of the other source functions, such as wind input and dissipation, must be improved. We believe that the use of accurate methods for evaluating Snl, such as SRIAM, will lead to improvements in the representation of these terms for operational use. Then the estimated wave statistics and spectral shapes near Japan should be validated against observational data, such as buoy and satellite altimeter data. However, greater numbers of in situ directional wave measurement devices are desperately needed, as currently there are relatively few such devices operating in the open ocean.

As we have demonstrated, the use of a sophisticated numerical scheme for nonlinear transfer significantly modifies the shape of the directional spectrum. However, the forcing fields (i.e., wind and current fields) determine the overall spectral properties, and therefore, for accurate simulation, the quality of these forcing fields must be improved. We utilized the best ocean current data available: the JCOPE reanalysis data for the Kuroshio path near Japan (Miyazawa et al. 2005; Kagimoto et al. 2008). The effects of wave–current interactions were apparent only because the fine structure of the current field was well represented in this Kuroshio model.

The hindcast wave spectrum analysis provided new insights into the nature of wind waves in the ocean. Recent studies have suggested that when a wave loses directionality and becomes long crested, nonresonant wave–wave interactions cause the wave train to become unstable (Gramstad and Trulsen 2007; Waseda et al. 2009). Because Hasselmann's kinetic equation (Hasselmann 1963) assumes a random process, the phase information is averaged and the deterministic nonresonant interaction is ruled out. Nevertheless, third-generation wave models are useful for predicting freak waves because they can predict the occurrence of an extreme condition when wave spectra lose directionality. A companion paper by Waseda et al. (2009) discusses the likelihood of such a sea state based on the wave hindcast results described in this paper. Localized regions or "hotspots" of freak-wave occurrence were identified, but their existence was limited both in duration and area. Thus, it is apparent that the success of freak-wave prediction relies heavily on the accuracy of the high-resolution current and wind fields as well as the performance of the wave model in response to the temporal and spatial variation of these forcing fields.

The performance of the wave model was significantly improved by using SRIAM. The computational cost is larger than the costs of existing operational models using DIA (~20 times), but we believe that the improvement gained by using sophisticated nonlinear transfer estimation is significant. We therefore recommend that SRIAM be incorporated into operational wave-forecasting models as available computational resources advance.

Acknowledgments. This work is part of the Japan Coastal Ocean Predictability Experiment (JCOPE) started in October 1997 under the initiative of the Frontier Research System for Global Change (FRSGC), which is supported by the Japan Agency for Marine-Earth Science and Technology (JAMSTEC). We are grateful to Dr. Takashi Kagimoto (FRCGC) who provided many valuable comments.

APPENDIX

Numerical Schemes for Time Integration of Source Terms

To implement RIAM and SRIAM in an operational third-generation wave model, either a semi-implicit or an implicit scheme should be applied for time integration to reduce computational time by using a larger time increment. WW3 uses a fractional step method in which the propagation and source terms are integrated separately. With the propagation terms excluded, the equation describing the evolution of wave action density $N(\mathbf{k})$ becomes

$$\frac{N^{n+1}(\mathbf{k}) - N^{n}(\mathbf{k})}{\Delta t} = (1 - \alpha)S^{n} + \alpha S^{n+1}, \qquad \text{(A1)}$$

where n is the index of time level, Δt is the time step, $\mathbf{k}$ is the wavenumber vector, S (N) is the total source term defined for the action spectrum, and α is the implicitness parameter. If the source term S^{n+1} depends linearly on N^{n+1}, Eq. (A1) can be solved directly for wave action at the new time step. In general, S^{n+1} depends nonlinearly on wave action density. Therefore, S^{n+1} was evaluated using a first-order Taylor series expansion around S^{n}:

$$S^{n+1}(\mathbf{k}) = S^{n}(\mathbf{k}) + \sum_{\mathbf{k}'} \frac{\partial S(\mathbf{k})}{\partial N(\mathbf{k}')}[N^{n+1}(\mathbf{k}') - N^{n}(\mathbf{k}')]. \qquad \text{(A2)}$$

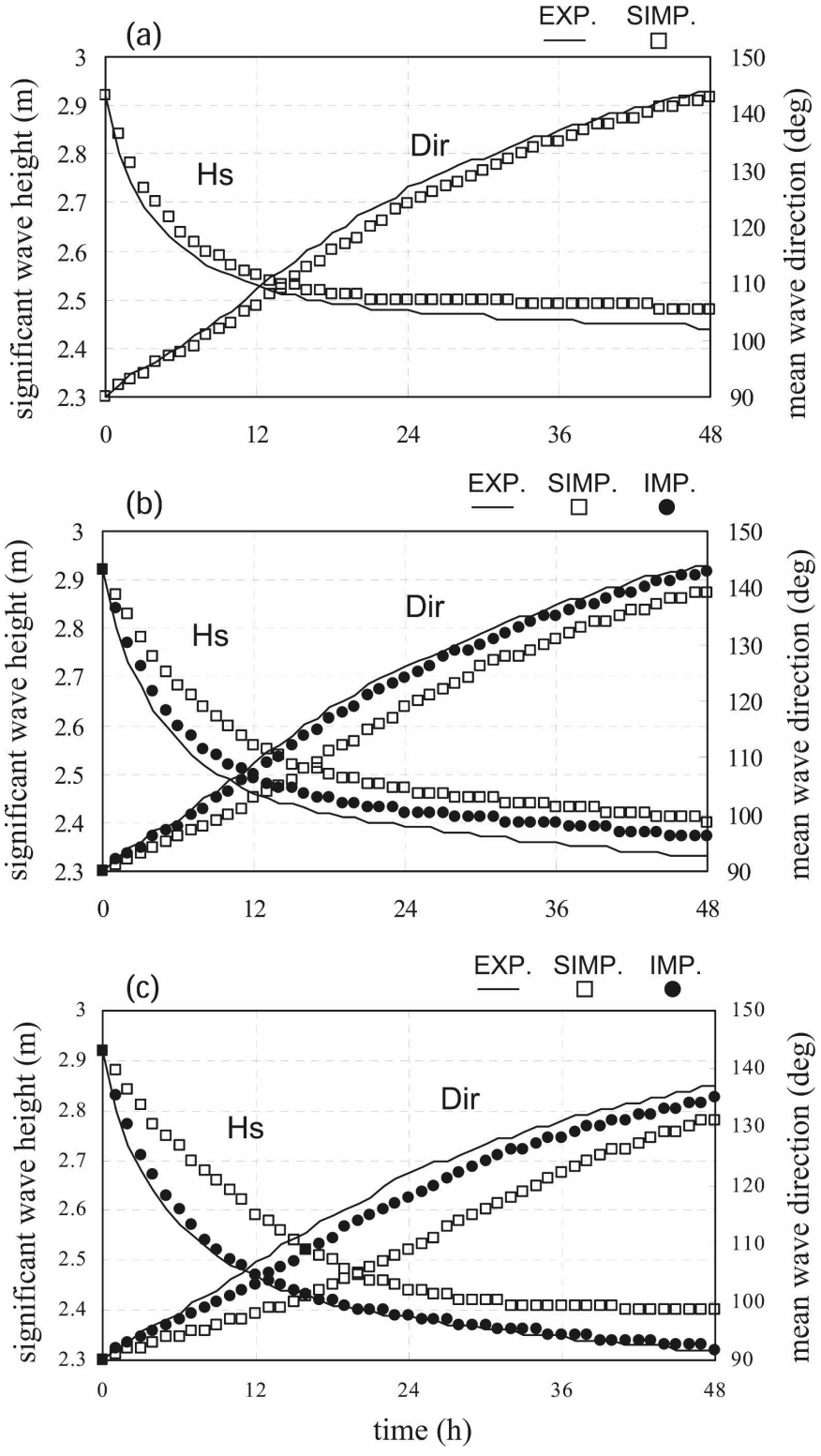

FIG. A1. Time evolution of significant wave height and mean wave direction calculated by (a) DIA, (b) SRIAM, and (c) RIAM as the nonlinear transfer function. Thin line: explicit scheme, □: semi-implicit scheme, ●: implicit scheme.

In a discretized form, the functional derivative $\partial S/\partial N$ becomes the Jacobian matrix of first-order partial derivatives of S with respect to N. The functional derivative can be divided into a diagonal matrix and a nondiagonal residual that is generally neglected in third-generation wave models such as WAM and WW3:

$$S^{n+1}(\mathbf{k}) = S^{n}(\mathbf{k}) + \frac{\partial S(\mathbf{k})}{\partial N(\mathbf{k})}\Delta N^{n}(\mathbf{k}). \qquad \text{(A3)}$$

Substituting (A3) into (A1), wave action density after a finite time interval Δt can be expressed as follows:

$$N^{n+1}(\mathbf{k}) = N^{n}(\mathbf{k}) + \frac{\Delta t \cdot S(\mathbf{k})}{1 - \alpha \cdot \Lambda(\mathbf{k}) \cdot \Delta t}, \qquad \text{(A4)}$$

where $\Lambda(\mathbf{k})$ represents the diagonal terms of $\partial S(\mathbf{k})/\partial N(\mathbf{k}')$. When the implicitness parameter α is set to 0, this method becomes the explicit Euler method. On the other hand, when α is set to 1, this method becomes the implicit Euler method, whereas the action density of the next time step is evaluated only with the quantities of the present time step (Hargreaves and Annan 2001). This semi-implicit scheme does not need matrix inversion to solve the equation. Therefore, it reduces computational cost significantly. Because the contribution of nondiagonal terms is sufficiently small (WAMDI Group 1988; Komen et al. 1994), this scheme has been successfully applied to third-generation wave models in which the DIA is used as the Snl.

To investigate the applicability of this integration scheme to RIAM and SRIAM, we conducted numerical simulations. The accuracy of the scheme was examined by referring to the results of the explicit scheme ($\alpha = 0$) with a small time increment (5 s), considering that the use of such small time steps increases the computational costs considerably. We also applied an implicit numerical scheme described by Lavrenov (2003) as a possible candidate for time integration of RIAM and SRIAM.

A numerical simulation was performed for a wind field in which the wind direction changes abruptly from the initial direction. Spectral evolution was calculated for a one-grid duration-limited condition. The initial wave spectrum was a standard JONSWAP spectrum with $\cos^2\theta$-type directional spreading. At the beginning of time integration, wind speed dropped to 10 m s^{-1} while the wind direction turned by 90° from the initial mean wave direction.

Figures A1a–c indicate the evolution of the significant wave height and mean wave direction calculated by DIA, SRIAM, and RIAM, respectively. As reported by WAMDI Group (1988) and Komen et al. (1994), the results calculated by DIA using the semi-implicit scheme were nearly the same as those of the explicit scheme, indicating that the contribution of nondiagonal terms is negligible compared to that of the diagonal terms. However, the difference between the explicit and semi-implicit schemes is apparent for SRIAM and especially for RIAM. The rate of change for the two parameters was slow for the semi-implicit scheme, showing a gradual transition of the wave spectrum for the new wind direction. On the other hand, the implicit scheme applied to SRIAM and RIAM reproduced the results of the explicit scheme. These results indicate that the discrepancy between the integration schemes was caused by inadequate use of the semi-implicit scheme with SRIAM and RIAM.

REFERENCES

Banner, M. L., and I. R. Young, 1994: Modeling spectral dissipation in the evolution of wind waves. Part I: Assessment of existing model performance. *J. Phys. Oceanogr.,* **24,** 1550–1571.

Bidlot, J., P. E. A. M. Janssen, and S. Abdalla, 2007: A revised formulation of ocean wave dissipation and its model impact. ECMWF Tech. Memo. 509, 29 pp.

Gramstad, O., and K. Trulsen, 2007: Influence of crest and group length on the occurrence of freak waves. *J. Fluid Mech.,* **582,** 463–472, doi:10.1017/S0022112007006507.

Guo, X., H. Hukuda, Y. Miyazawa, and T. Yamagata, 2003: A triply nested ocean model simulating the Kuroshio—Roles of horizontal resolution on JEBAR. *J. Phys. Oceanogr.,* **33,** 146–169.

Hargreaves, J. C., and J. D. Annan, 2001: Comments on improvement of short fetch behavior in the WAM model. *J. Atmos. Oceanic Technol.,* **18,** 711–715.

Hasselmann, K., 1963: On the non-linear energy transfer in a gravity-wave spectrum. Part 2. Conservation theorems; wave-particle analogy; irreversibility. *J. Fluid Mech.,* **15,** 273–281.

Hasselmann, S., K. Hasselmann, J. H. Allender, and T. P. Barnett, 1985: Computations and parameterizations of the nonlinear energy transfer in a gravity-wave spectrum. Part II: Parameterizations of the nonlinear energy transfer for application in wave models. *J. Phys. Oceanogr.,* **15,** 1378–1391.

Holthuijsen, L. H., and H. L. Tolman, 1991: Effects of the Gulf Stream in ocean waves. *J. Geophys. Res.,* **96,** 12 755–12 771.

Hubbert, K. P., and J. Wolf, 1991: Numerical investigation of depth and current refraction of waves. *J. Geophys. Res.,* **96,** 2737–2748.

Hwang, P. A., 2005: Altimeter measurements of wind and wave modulation by the Kuroshio in the Yellow and East China Seas. *J. Oceanogr.,* **61,** 987–993.

Janssen, P. A. E. M., 2003: Nonlinear four-wave interactions and freak waves. *J. Phys. Oceanogr.,* **33,** 863–884.

——, J. Bidlot, S. Abdalla, and H. Hersbach, 2005: Progress in ocean wave forecasting at ECMWF. ECMWF Tech. Memo. 478, 28 pp.

Jonsson, I. G., 1990: Wave-current interactions. *The Sea,* B. Le Mehaute and D. M. Hanes, Eds., Ocean Engineering Science, Vol. 9A, Wiley-Interscience, 65–120.

Kagimoto, T., Y. Miyazawa, X. Guo, and H. Kawajiri, 2008: High resolution Kuroshio forecast system: Description and its ap-

plications. *High Resolution Numerical Modeling of the Atmosphere and Ocean,* W. Ohfuchi and K. Hamilton, Eds., Springer, 209–234.

Kahma, K. K., and C. J. Calkoen, 1994: Growth curve observations. *Dynamics and Modelling of Ocean Waves*, G. J. Komen et al., Eds., Cambridge University Press, 174–182.

Kenyon, K. E., 1971: Wave refraction in ocean currents. *Deep-Sea Res.,* **18,** 1023–1033.

Komatsu, K., 1996: Development of a new generation wave forecasting model based on a new schema of nonlinear energy transfer among wind waves (in Japanese). Ph.D. thesis, Kyushu University, 155 pp.

——, and A. Masuda, 1996: A new scheme of nonlinear energy transfer among wind waves: RIAM method—Algorithm and performance. *J. Oceanogr.,* **52,** 509–537.

Komen, G. J., K. Hasselmann, and S. Hasselmann, 1984: On the existence of a fully developed wind-sea spectrum. *J. Phys. Oceanogr.,* **14,** 1271–1285.

——, L. Cavaleri, M. Donelan, K. Hasselmann, S. Hasselmann, and P. E. A. M. Janssen, 1994: *Dynamics and Modelling of Ocean Waves*. Cambridge University Press, 532 pp.

Lavrenov, I., 1998: The wave energy concentration at the Agulhas current of South Africa. *Nat. Hazards,* **17,** 117–127.

——, 2003: *Wind-Waves in Oceans: Dynamics and Numerical Simulations*. Springer, 377 pp.

Masson, D., 1996: A case study of wave-current interactions in a strong tidal current. *J. Phys. Oceanogr.,* **26,** 359–372.

Masuda, A., 1980: Nonlinear energy transfer between wind waves. *J. Phys. Oceanogr.,* **10,** 2082–2093.

Mathiesen, M., 1987: Wave refraction by a current whirl. *J. Geophys. Res.,* **92,** 3905–3912.

Mei, C. C., 1989: *Applied Dynamics of Ocean Surface Waves*. 2nd ed. World Scientific, 740 pp.

Miyazawa, Y., S. Yamane, X. Guo, and T. Yamagata, 2005: Ensemble forecast of the Kuroshio meandering. *J. Geophys. Res.,* **110,** C10026, doi:10.1029/2004JC002426.

Onorato, M., A. R. Osborne, M. Serio, L. Cavaleri, C. Brandini, and C. T. Stansberg, 2004: Observation of strongly non-Gaussian statistics for random sea surface gravity waves in wave flume experiments. *Phys. Rev. E,* **70,** doi:10.1103/PhysRevE.70.067302.

Resio, D. T., and W. Perrie, 1991: A numerical study of nonlinear energy fluxes due to wave-wave interactions. Part 1: Methodology and basic results. *J. Fluid Mech.,* **223,** 609–629.

Snyder, R. L., F. W. Dobson, J. A. Elliott, and R. B. Long, 1981: Array measurements of atmospheric pressure fluctuations above surface gravity waves. *J. Fluid Mech.,* **102,** 1–59.

Tolman, H. L., 1990: The influence of unsteady depths and currents of tides on wind-wave propagation in shelf seas. *J. Phys. Oceanogr.,* **20,** 1166–1174.

——, 1991: Effects of tides and storm surges on North Sea wind waves. *J. Phys. Oceanogr.,* **21,** 766–781.

——, 1992: Effects of numerics on the physics in a third-generation wind-wave model. *J. Phys. Oceanogr.,* **22,** 1095–1111.

——, 2002: User manual and system documentation of WAVEWATCH-III, version 2.22. NOAA/NWS/NCEP/MMAB Tech. Note 222, 133 pp.

——, and D. V. Chalikov, 1996: Source terms in a third-generation wind-wave model. *J. Phys. Oceanogr.,* **26,** 2497–2518.

Van Vledder, G. Ph., 2006: The WRT method for the computation of non-linear four-wave interactions in discrete spectral wave models. *Coastal Eng.,* **53,** 223–242.

WAMDI Group, 1988: The WAM model—A third generation ocean wave prediction model. *J. Phys. Oceanogr.,* **18,** 1775–1810.

Wang, D. W., A. K. Liu, C. Y. Peng, and E. A. Meindl, 1994: Wave-current interaction near the Gulf Stream during the surface wave dynamics experiment. *J. Geophys. Res.,* **99,** 5065–5079.

Waseda, T., T. Kinoshita, and H. Tamura, 2009: Evolution of a random directional wave and freak wave occurrence. *J. Phys. Oceanogr.,* in press.

White, B. S., and B. Fornberg, 1998: On the chance of freak waves at the sea. *J. Fluid Mech.,* **255,** 113–138.

Wolf, J., 2003: BNSC NEWTON Project: Along track interferometry for ocean currents and swell. Tech. Note 6: Wave-Current Modelling (WP30): Phase 2 (Kuroshio), Proudman Oceanographic Laboratory Internal Doc. 147, 23 pp.

Young, I. R., and G. Ph. Van Vledder, 1993: A review of the central role of nonlinear interactions in wind-wave evolution. *Trans. Roy. Soc. London,* **342,** 505–524.